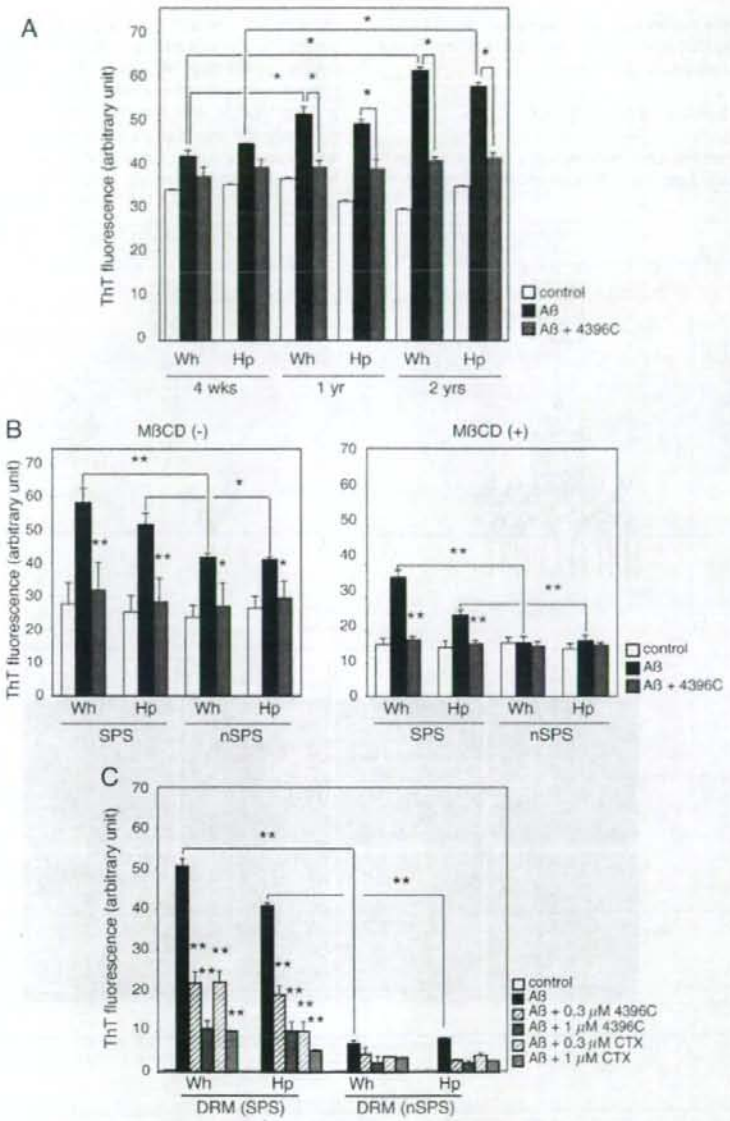

Fig. 4. Aβ assembly in the presence of DRM isolated from synaptosomes of aged mouse brain. (A) The ThT fluorescence intensity of the incubation mixtures containing Aβ incubated at 50 μM and 37 °C for 24 h in the presence or absence of synaptosomes prepared from brains of three different age groups of mice with or without 4396C is shown. (B) The ThT fluorescence intensity of the incubation mixtures containing Aβ incubated at 50 μM and 37 °C for 24 h in the presence or absence of synaptosomes or non-synaptosomes prepared from aged mouse brain with or without 4396C is shown. The synaptosomes and non-synaptosomes had been pretreated with or without MβCD. (C) The ThT fluorescence intensity of the incubation mixtures containing Aβ incubated at 50 μM and 37 °C for 24 in the presence or absence of DRM isolated from synaptosomes or non-synaptosomes of aged mouse brain with or without 4396C or CTX is shown. Each column indicates the average of four values±S.D. *$p<0.001$, **$p<0.0001$ (one-way ANOVA combined with Scheffe's test). SPS; synaptosome fraction, nSPS; non-synaptosome fraction, Wh: whole brain minus the hippocampus, cerebellum and brainstem, Hp: hippocampus.

the incubated mixtures containing the synaptosomes significantly increased compared with that in the incubation mixtures containing non-synaptosomes (Fig. 4B). Again, the increase in the ThT fluorescence intensity was significantly suppressed by coincubation with 4396C. Importantly, the increase in the ThT fluorescence intensity of the incubation mixture was not suppressed by MβCD pretreatment (Fig. 4B).

We then investigated whether the potency of synaptosomes to accelerate Aβ assembly is attributed to the DRMs. We incubated soluble Aβ1–40 in the presence of the isolated DRMs from synaptosomes or non-synaptosomes of aged mouse brain. The ThT fluorescence intensity significantly increased in the incubation mixtures containing the DRMs isolated from synaptosomes but not from non-synaptosomes (Fig. 4C). Again, the increase in the ThT fluorescence

intensity was significantly suppressed by coincubation with CTX or 4396C (Fig. 4C), indicating that amyloid fibril formation in the presence of DRMs is GM1-dependent and GAβ-mediated.

3.4. High-density GM1 clustering on synaptosomes

To further characterize the GM1 accumulation on the surface of synaptosomes, particularly from the viewpoint of GM1 clustering, we incubated the synaptosomes prepared from whole brain and hippocampus of young and aged mouse brains with a novel peptide (p3), which specifically recognizes the high-density GM1 clustering (Fig. 5A). The p3 binding was extremely restricted to synaptosomes and no binding was detected on non-synaptosomes (Fig. 5B). Importantly, the levels of p3 binding to synaptosomes prepared from aged mouse brains was significantly higher than those of p3 binding to synaptosomes prepared from young mouse brains (Fig. 5B, C).

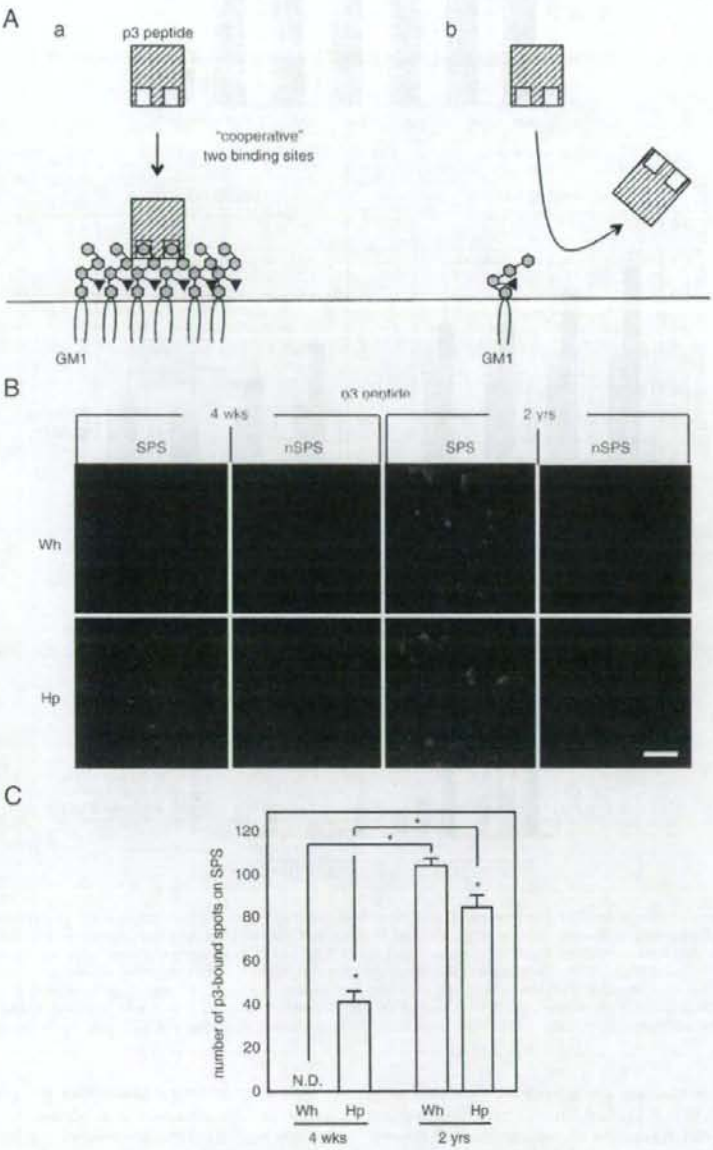

Fig. 5. Peptide p3 binds to synaptosome from aged mouse brain. (A) Proposed scheme for the specific p3 binding to GM1 clusters. (B) The synaptosomes and non-synaptosomes prepared from young (4-week-old) and aged (2-year-old) mouse brains were incubated with biotin-conjugated p3 then with Alexa Fluor 594-conjugated streptavidin. Bar, 50 μm. (C) The number of p3-bound spots shown in (B) was determined. Each column indicates the average of four values ± S.D. *$p<0.0001$ (one-way ANOVA combined with Scheffe's test). ND: not detected. SPS: synaptosome fraction, nSPS: non-synaptosome fraction, Wh: whole brain minus the hippocampus, cerebellum and brainstem, Hp: hippocampus.

Interestingly, in the experiment using synaptosomes obtained from young mouse brains, the p3 binding was only observed in those prepared from hippocampus but not from whole brain (Fig. 5B, C).

3.5. Age-dependent sphingomyelin accumulation in synaptosomes

To explore a possible mechanism of the age-dependent high-density GM1 clustering in synaptosomes, we examined the lipid composition of synaptosomes prepared from three different age groups of mice (4-week-old, 1-year-old and 2-year-old groups). Significantly, the SM levels, which were determined by thin-layer chromatography (TLC), increased with age in synaptosomes prepared from both whole brain and hippocampus (Fig. 6). The GM1 level in synaptosomes also increased with age but to a lesser extent than the increase in SM level, whereas the levels of cholesterol and total phospholipids in synaptosomes remained unchanged, except a decrease in the cholesterol content in the synaptosomes prepared from hippocampus, with age, respectively (Fig. 6). Then, to further characterize the age-dependent SM accumulation in the synaptosomes, we isolated DRMs from the synaptosomes and non-synaptosomes prepared from whole brain minus hippocampus, cerebellum and brainstem, and the hippocampus of aged mouse brains. The SM level was significantly higher in the DRMs isolated from synaptosomes than in those isolated from non-synaptosomes (Fig. 7). Enrichment in the DRMs isolated from synaptosomes was not observed with GM1, cholesterol and total phospholipids (Fig. 7).

3.6. Induction of high-density GM1 clustering at neuritic terminals through sphingomyelinase inhibition

To obtain direct evidence that SM is involved in the induction of high-density GM1 clustering, we incubated PC12 cells, which were induced to differentiate with nerve growth factor, with GW4869, which specifically inhibits plasma-membrane-bound neutral sphingomyelinase (nSMase). The SM levels following nSMase inhibition significantly increased whereas the GM1 levels apparently remained unchanged with the treatment (Fig. 8A). Notably, the p3 binding was specifically observed at neuritic terminals of the PC12 cells, and it was only observed when the cells were pretreated with GW4869. In contrast, the CTX binding at the neuritic terminals was consistently observed regardless of GW4869 pretreatment of the cells (Fig. 8B).

4. Discussion

A previous *in vitro* study using liposomes clearly showed that GM1-mediated Aβ fibril formation through GAβ generation significantly depends on the GM1 distribution but not merely on the GM1

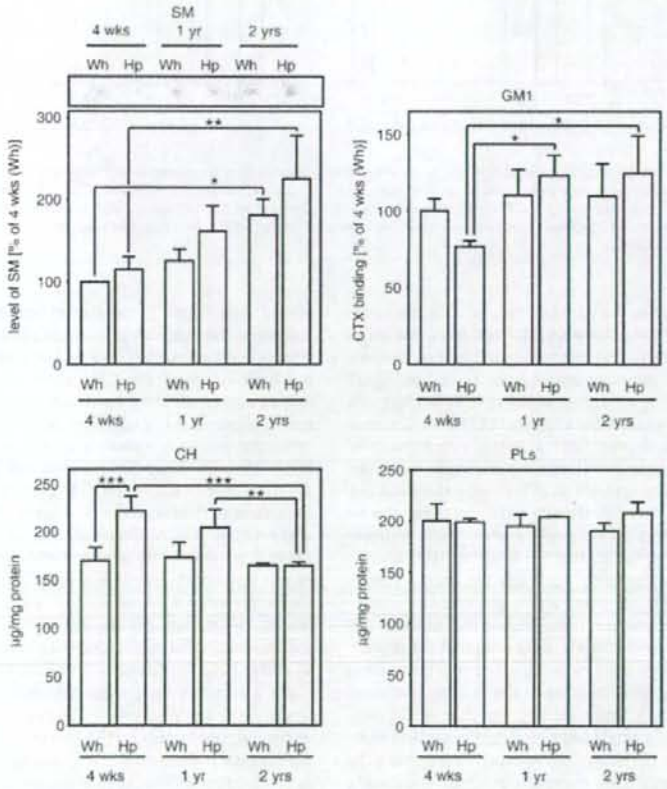

Fig. 6. Aging induces SM and GM1 accumulation in synaptosomes. The lipid composition of synaptosomes prepared from mouse brains of three different age groups is shown. The SM levels were determined by densitoscanning the TLC plate. The intensities of the bands relative to those of the 4-week-old mice are indicated. The GM1 levels were determined by densitoscanning the blot incubated with CTX-HRP. The intensities of the bands relative to those of the 4-week-old mice are indicated. The CH and PLs levels were determined using Determiner L and Phospholipids C, respectively. Each column indicates the average of eight values±S.D. *$p<0.05$, **$p<0.005$, ***$p<0.001$ (one-way ANOVA combined with Scheffe's test). Wh: whole brain minus the hippocampus, cerebellum and brainstem, Hp: hippocampus.

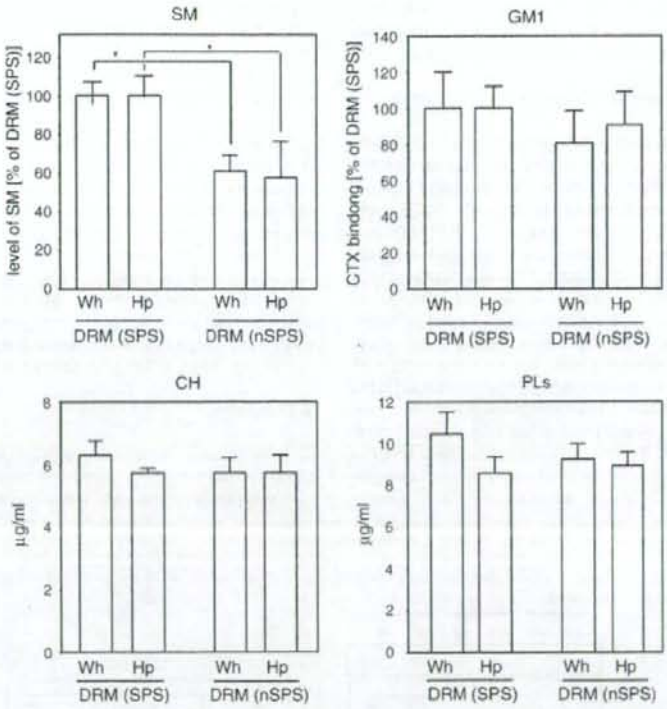

Fig. 7. Lipid composition of DRM isolated from synaptosomes. The lipid composition of DRM isolated from synaptosomes and non-synaptosomes prepared from aged (2-year-old) mouse brain is shown. The SM and GM1 levels were determined by densitoscanning the TLC plate and the blot incubated with CTX-HRP, respectively. The intensities of the bands relative to those of synaptosomes are indicated. The CH and PLs levels were determined using Determiner L and Phospholipids C, respectively. Each column indicates the average of four values ±S.D. *$p<0.001$ (one-way ANOVA combined with Scheffe's test). SPS: synaptosome fraction, nSPS: non-synaptosome fraction, Wh: whole brain minus the hippocampus, cerebellum and brainstem, Hp: hippocampus.

level in the membranes; that is, the Aβ fibril formation is markedly facilitated in the presence of GM1 clusters [13]. Thus, it is a challenge to determine how the GM1 clustering, to the extent that it accelerates GAβ generation, occurs on neuronal membranes under biological conditions. In this study, taking advantage of the specific binding of a novel peptide, p3, to high-density GM1 clusters [24,30], we successfully showed that the high-density GM1 clusters, which potently induce Aβ fibrillogenesis, appeared with age at presynaptic terminals in the brain. This study also suggested that the age-dependent SM accumulation is involved in the high-density GM1 clustering at presynaptic terminals. Our results may provide a new insight into the biological mechanism of Aβ assembly into fibrils in the AD brain.

The novel peptide, p3, has recently been selected from a phage-displayed random peptide library using air–water interface monolayers [24]. From the Hill plot analysis, it was shown that p3 likely has two binding sites that work cooperatively, indicating that the peptide p3 simultaneously binds to two GM1 molecules that stand very close to each other [24]. This is in good contrast to the binding feature of CTX to GM1, where CTX has a single binding site that works non-cooperatively and equally to a single GM1 molecule regardless of its standing whether solitary or in cluster [24]. Although it remains to be clarified how the high-density GM1 clustering provides a favorable microenvironment for GAβ generation, it may be assumed that the alteration of GM1 lateral distribution affects the spatial arrangement of the oligosaccharide chain (head-group) of the GM1 molecule [31].

One of the striking findings of this study is that the high-density GM1 clustering was exclusively observed in synaptosomes but not in non-synaptosomes. To the best of our knowledge, no study has ever compared the lipid composition of DRMs, particularly the GM1 level, between synaptosomes and non-synaptosomes. Further studies are required; however, the GM1 turnover at presynaptic neuritic terminals may be different from that at other neuronal membranes. The result of our recent study is in line with this possibility. That is, the endocytic pathway abnormality that was induced by treatment of PC12 cells with chloroquine, a weak base, facilitated the GM1-induced Aβ fibrillogenesis selectively at presynaptic neuritic terminals [32] regardless of the broad distribution of GM1 throughout the cell body and neurites [33]. Alternatively, the GM1 distribution at presynaptic neuritic terminals may be modified by other membrane constituents. In this context, this study showed that SM preferably localized in the DRMs prepared from synaptosomes compared with in those from non-synaptosomes. It is also interesting to note that the maturation of the axonal plasma membrane is associated with increasing SM levels in DRMs [34]. Furthermore, in terms of the MβCD resistance of the GMD, a previous study suggested that the SM level in a given membrane plays a critical role in the retention of cholesterol against the efflux induced by MβCD [35]. This line of evidence suggests that SM at presynaptic plasma membranes, the level of which increases with age, is involved in the formation of unique membrane microdomains such as the GMD. A previous study also suggested that cholesterol plays a critical role in the formation of GMD, which is responsible for GAβ-induced Aβ assembly [13]. However, we did not observe an age-dependent increase in the cholesterol level in synaptosomes as previously reported [36,37]. At present, the reason for the discrepancy

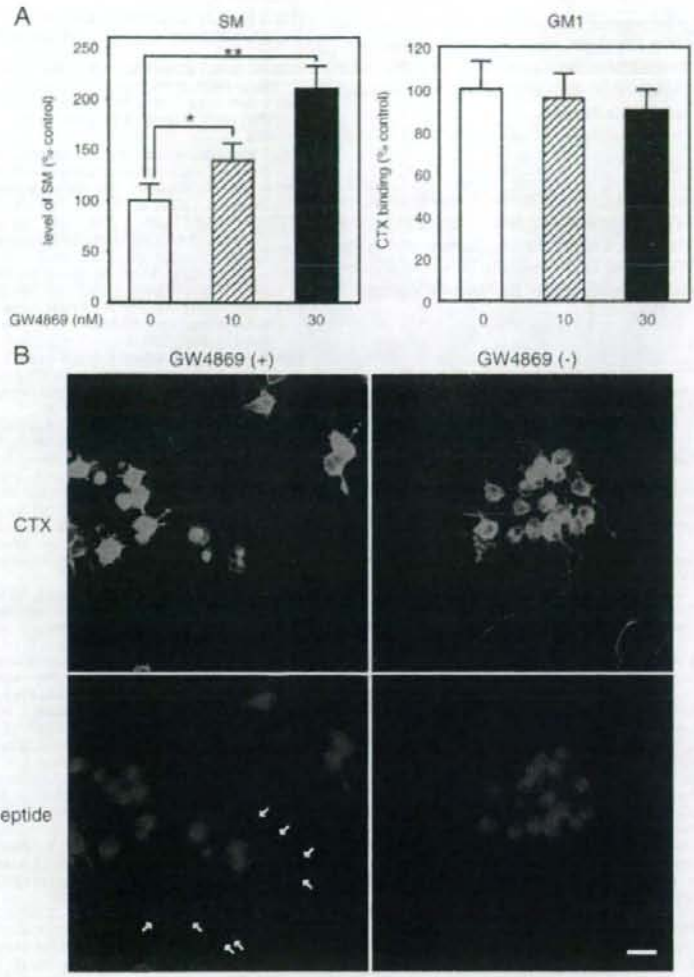

Fig. 8. High-density GM1 clustering at neuritic terminals through sphingomyelinase inhibition. (A) PC12 cells were treated with GW4869 at the indicated concentrations for 2 days. The SM and GM1 levels were determined by densitoscanning the TLC plates and the blot incubated with CTX-HRP, respectively. The intensities of the bands relative to those of the control are indicated. Each column indicates the average of four values ± S.D. $^{*}p < 0.01$, $^{**}p < 0.001$ (one-way ANOVA combined with Scheffe's test). (B) Fluorescence image of GW4869-treated or untreated PC12 cells with CTX (green) and p3 (red) is shown. Arrows indicate the neuritic terminals of PC12 cells. Bar, 100 μm.

in results between this study and previous studies remains unclear. Studies in the future should clarify whether cholesterol level in synaptosomes can be affected by age and other various factors such as feed, and also whether its age-dependent alteration can influence the formation of GMD in the brain.

Although this study was limited to the hippocampus and whole brain minus the hippocampus of mouse brains, the favorable appearance of high-density GM1 clusters in the hippocampus may imply its pathological significance because the hippocampus is an invariably preferable region for Aβ deposition in various transgenic mouse brains [38–40]. Our previous study using cultured primary neurons showed that the lipid composition and lipid requirement for differentiation were different between hippocampal neurons and cortical neurons; that is, the cholesterol levels of hippocampal neurons are significantly higher than those of cortical neurons [41]. The implication of this study to address the pathophysiology of AD is limited because our data were obtained only from animals; however, this study may raise particular concerns on the significance of the alteration of the composition and distribution of lipids, including GM1, SM and cholesterol at presynaptic plasma membranes in relation to the initiation of amyloid pathology associated with AD.

In summary, our results suggest that high-density GM1 clustering, which markedly induces Aβ assembly, occurs in presynaptic neuritic terminals in the brain in age-dependent, and partially, brain-region-specific manners. It was previously reported that Aβ deposition starts at the presynaptic neuritic terminals in AD brain [21,22] and that the GM1 levels significantly increase in the DRMs [42] and also in amyloid-positive synaptosomes prepared from AD brain [23]. With this evidence, our results suggest that the age-dependent GM1 accumulation to its high-density clustering in presynaptic neuritic terminals is a critical step for Aβ deposition in AD. Recently, accumulated evidence has indicated that amyloid fibril formation from various amyloidogenic proteins other

than Aβ, including IAPP, prion protein, calcitonin and SAA, is accelerated through their interaction with biomembranes, conversely, the biomembrane structure is likely affected by amyloid growth [43–48]. This study may also provide a novel insight into molecular pathogenesis common among various amyloid-generating diseases.

Acknowledgements

This study was supported by a Grant-in-Aid for Scientific Research on Priority Areas Research on Pathomechanisms of Brain Disorders from the Ministry of Education, Culture, Sports, Science and Technology of Japan (1700220004) and by the Program for the Promotion of Fundamental Studies in Health Sciences of the National Institute of Biomedical Innovation (NIBIO).

References

[1] E. Terzi, G. Holzemann, J. Seelig, Alzheimer b-amyloid peptide 25–35: electrostatic interactions with phospholipid membranes, Biochemistry 33 (1994) 7434–7441.
[2] E. Terzi, G. Holzemann, J. Seelig, Self-association of b-amyloid peptide (1–40) in solution and binding to lipid membranes, J. Mol. Biol. 252 (1995) 633–642.
[3] C.M. Yip, J. McLaurin, Amyloid-b peptide assembly: a critical step in fibrillogenesis and membrane disruption, Biophys. J. 80 (2001) 1359–1371.
[4] N.A. Avdulov, S.V. Chochina, U. Igbavboa, C.S. Warden, A.V. Vassiliev, W.G. Wood, Lipid binding to amyloid b-peptide aggregates: preferential binding of cholesterol as compared with phosphatidylcholine and fatty acids, J. Neurochem. 69 (1997) 1746–1752.
[5] C.M. Yip, E.A. Elton, A.A. Darabie, M.R. Morrison, J. McLaurin, Cholesterol, a modulator of membrane-associated Ab-fibrillogenesis and neurotoxicity, J. Mol. Biol. 311 (2001) 723–734.
[6] G.P. Eckert, C. Kirsch, S. Leutz, W.G. Wood, W.E. Müller, Cholesterol modulates amyloid beta-peptide's membrane interactions, Pharmacopsychiatry (Suppl 2) (2003) S136–S143.
[7] K. Yanagisawa, A. Odaka, N. Suzuki, Y. Ihara, GM1 ganglioside-bound amyloid b-protein (Ab): a possible form of preamyloid in Alzheimer's disease, Nat. Med. 1 (1995) 1062–1066.
[8] K. Yanagisawa, Y. Ihara, GM1 ganglioside-bound amyloid b-protein in Alzheimer's disease brain, Neurobiol. Aging 19 (1998) S65–S67.
[9] J. McLaurin, A. Chakrabartty, Membrane disruption by Alzheimer b-amyloid peptides mediated through specific binding to either phospholipids or gangliosides. Implications for neurotoxicity, J. Biol. Chem. 271 (1996) 26482–26489.
[10] L.P. Choo-Smith, W.K. Surewicz, The interaction between Alzheimer amyloid b (1–40) peptide and ganglioside GM1-containing membranes, FEBS Lett. 402 (1997) 95–98.
[11] L.P. Choo-Smith, W. Garzon-Rodriguez, C.G. Glabe, W.K. Surewicz, Acceleration of amyloid fibril formation by specific binding of Ab-(1–40) peptide to ganglioside-containing membrane vesicles, J. Biol. Chem. 272 (1997) 22987–22990.
[12] K. Matsuzaki, C. Horikiri, Interactions of amyloid b-peptide (1–40) with ganglioside-containing membranes, Biochemistry 38 (1999) 4137–4142.
[13] A. Kakio, S.I. Nishimoto, K. Yanagisawa, Y. Kozutsumi, K. Matsuzaki, Cholesterol-dependent formation of GM1 ganglioside-bound amyloid b-protein, an endogenous seed for Alzheimer amyloid, J. Biol. Chem. 276 (2001) 24985–24990.
[14] A. Kakio, S. Nishimoto, K. Yanagisawa, Y. Kozutsumi, K. Matsuzaki, Interactions of amyloid b-protein with various gangliosides in raft-like membranes: importance of GM1 ganglioside-bound form as an endogenous seed for Alzheimer amyloid, Biochemistry 41 (2002) 7385–7390.
[15] H. Hayashi, N. Kimura, H. Yamaguchi, K. Hasegawa, T. Yokoseki, M. Shibata, N. Yamamoto, M. Michikawa, Y. Yoshikawa, K. Terao, K. Matsuzaki, C.A. Lemere, D.J. Selkoe, H. Naiki, K. Yanagisawa, A seed for Alzheimer amyloid in the brain, J. Neurosci. 24 (2004) 4894–4902.
[16] M. Wakabayashi, T. Okada, Y. Kozutsumi, K. Matsuzaki, GM1 ganglioside-mediated accumulation of amyloid b-protein on cell membranes, Biochem. Biophys. Res. Commun. 328 (2005) 1019–1023.
[17] N. Yamamoto, T. Yokoseki, M. Shibata, H. Yamaguchi, K. Yanagisawa, Suppression of Ab deposition in brain by peripheral administration of Fab fragments of anti-seed antibody, Biochem. Biophys. Res. Commun. 335 (2005) 45–47.
[18] N. Yamamoto, U. Igbabvoa, Y. Shimada, Y. Ohno-Iwashita, M. Kobayashi, W.G. Wood, S.C. Fujita, K. Yanagisawa, Accelerated Ab aggregation in the presence of GM1-ganglioside-accumulated synaptosomes of aged apoE4-knock-in mouse brain, FEBS Lett. 569 (2004) 135–139.
[19] P. Scheiffele, M.G. Roth, K. Simons, Interaction of influenza virus haemagglutinin with sphingolipid-cholesterol membrane domains via its transmembrane domain, Embo J. 16 (1997) 5501–5508.
[20] S. Ilangumaran, D.C. Hoessli, Effects of cholesterol depletion by cyclodextrin on the sphingolipid microdomains of the plasma membrane, Biochem. J. 335 (Pt 2) (1998) 433–440.
[21] O. Bugiani, G. Giaccone, L. Verga, B. Pollo, B. Ghetti, B. Frangione, F. Tagliavini, Alzheimer patients and Down patients: abnormal presynaptic terminals are related to cerebral preamyloid deposits, Neurosci. Lett. 119 (1990) 56–59.
[22] A. Probst, D. Langui, S. Ipsen, N. Robakis, J. Ulrich, Deposition of beta/A4 protein along neuronal plasma membranes in diffuse senile plaques, Acta Neuropathol 83 (1991) 21–29.
[23] K.H. Gylys, J.A. Fein, F. Yang, C.A. Miller, G.M. Cole, Increased cholesterol in Ab-positive nerve terminals from Alzheimer's disease cortex, Neurobiol. Aging. 28 (2007) 8–17.
[24] T. Matsubara, K. Iijima, M. Nakamura, T. Taki, Y. Okahata, T. Sato, Specific binding of GM1-binding peptides to high-density GM1 in lipid membranes, Langmuir 23 (2007) 708–714.
[25] F. Schroeder, W.J. Morrison, C. Gorka, W.G. Wood, Transbilayer effects of ethanol on fluidity of brain membrane leaflets, Biochim. Biophys. Acta. 946 (1988) 85–94.
[26] U. Igbavboa, G.P. Eckert, T.M. Malo, A.E. Studniski, L.N. Johnson, N. Yamamoto, M. Kobayashi, S.C. Fujita, T.R. Appel, W.E. Muller, W.G. Wood, K. Yanagisawa, Murine synaptosomal lipid raft protein and lipid composition are altered by expression of human apoE 3 and 4 and by increasing age, J. Neurol. Sci. 229–230 (2005) 225–232.
[27] H. Naiki, F. Gejyo, Kinetic analysis of amyloid fibril formation, Methods Enzymol. 309 (1999) 305–318.
[28] F. Buss, M. Stewart, Macromolecular interactions in the nucleoproin p62 complex of rat nuclear pores: binding of nucleoporin p54 to the rod domain of p62, J. Cell Biol. 128 (1995) 251–261.
[29] N. Yamamoto, K. Yoneda, K. Asai, K. Sobue, T. Tada, Y. Fujita, H. Katsuya, M. Fujita, N. Aihara, M. Mase, K. Yamada, Y. Miura, T. Kato, Alterations in the expression of the AQP family in cultured rat astrocytes during hypoxia and reoxygeneration, Brain Res. Mol. Brain Res. 90 (2001) 26–38.
[30] T. Matsubara, D. Ishikawa, T. Taki, Y. Okahata, T. Sato, Selection of ganglioside GM1-binding peptides by using a phage library, FEBS Lett. 456 (1999) 253–256.
[31] P. Brocca, P. Berthault, S. Sonnino, Conformation of the oligosaccharide chain of G(M1) ganglioside in a carbohydrate-enriched surface, Biophys. J. 74 (1998) 309–318.
[32] K. Yuyama, N. Yamamoto, K. Yanagisawa, Chloroquine-induced endocytic pathway abnormalities: Cellular model of GM1 ganglioside-induced Ab fibrillogenesis in Alzheimer's disease, FEBS Lett. 580 (2006) 6972–6976.
[33] N. Yamamoto, Y. Fukata, M. Fukata, K. Yanagisawa, GM1-ganglioside-induced Ab assembly on synaptic membranes of cultured neurons, Biochim. Biophys. Acta. 1768 (2007) 1128–1137.
[34] M.D. Ledesma, B. Brugger, C. Bunning, F.T. Wieland, C.G. Dotti, Maturation of the axonal plasma membrane requires upregulation of sphingomyelin synthesis and formation of protein–lipid complexes, Embo J. 18 (1999) 1761–1771.
[35] M. Fukasawa, M. Nishijima, H. Itabe, T. Takano, K. Hanada, Reduction of sphingomyelin level without accumulation of ceramide in Chinese hamster ovary cells affects detergent-resistant membrane domains and enhances cellular cholesterol efflux to methyl-b-cyclodextrin, J. Biol. Chem. 275 (2000) 34028–34034.
[36] K. Nagy, V. Nagy, C. Bertoni-Freddari, I. Nagy, Alterations of the synaptosomal membrane 'microviscosity' in the brain cortex of rats during aging and centrophenoxine treatment, Arch. Gerontol. Geriatr. 2 (1983) 23–39.
[37] W.G. Wood, R. Strong, L.S. Williamson, R.W. Wise, Changes in lipid composition of cortical synaptosomes from different age groups of mice, Life Sci. 35 (1984) 1947–1952.
[38] K. Hsiao, P. Chapman, S. Nilsen, C. Eckman, Y. Harigaya, S. Younkin, F. Yang, G. Cole, Correlative memory deficits, Ab elevation, and amyloid plaques in transgenic mice, Science 274 (1996) 99–102.
[39] J. Nalbantoglu, G. Tirado-Santiago, A. Lahsaini, J. Poirier, O. Goncalves, G. Verge, F. Momoli, S.A. Welner, G. Massicotte, J.P. Julien, M.L. Shapiro, Impaired learning and LTP in mice expressing the carboxy terminus of the Alzheimer amyloid precursor protein, Nature 387 (1997) 500–505.
[40] G. Chen, K.S. Chen, J. Knox, J. Inglis, A. Bernard, S.J. Martin, A. Justice, L. McConlogue, D. Games, S.B. Freedman, R.G. Morris, A learning deficit related to age and b-amyloid plaques in a mouse model of Alzheimer's disease, Nature 408 (2000) 975–979.
[41] M. Ko, K. Zou, H. Minagawa, W. Yu, J.S. Gong, K. Yanagisawa, M. Michikawa, Cholesterol-mediated neurite outgrowth is differently regulated between cortical and hippocampal neurons, J. Biol. Chem. 280 (2005) 42759–42765.
[42] M. Molander-Melin, K. Blennow, N. Bogdanovic, B. Dellheden, J.E. Mansson, P. Fredman, Structural membrane alterations in Alzheimer brains found to be associated with regional disease development; increased density of gangliosides GM1 and GM2 and loss of cholesterol in detergent-resistant membrane domains, J. Neurochem. 92 (2005) 171–182.
[43] M. Reches, Y. Porat, E. Gazit, Amyloid fibril formation by pentapeptide and tetrapeptide fragments of human calcitonin, J. Biol. Chem. 277 (2002) 35475–35480.
[44] A. Mascioni, F. Porcelli, U. Ilangovan, A. Ramamoorthy, G. Veglia, Conformational preferences of the amylin nucleation site in SDS micelles: an NMR study, Biopolymers. 69 (2003) 29–41.
[45] G.P. Gellermann, T.R. Appel, A. Tannert, A. Radestock, P. Hortschansky, V. Schroeckh, C. Leisner, T. Lutkepohl, S. Shtrasburg, C. Rocken, M. Pras, R.P. Linke, S. Diekmann, M. Fandrich, Raft lipids as common components of human extracellular amyloid fibrils, Proc. Natl. Acad. Sci. U. S. A. 102 (2005) 6297–6302.
[46] T. Miura, M. Yoda, N. Takaku, T. Hirose, H. Takeuchi, Clustered negative charges on the lipid membrane surface induce b-sheet formation of prion protein fragment 106–126, Biochemistry 46 (2007) 11589–11597.
[47] J.R. Brender, U.H. Durr, D. Heyl, M.B. Budarapu, A. Ramamoorthy, Membrane fragmentation by an amyloidogenic fragment of human islet amyloid polypeptide detected by solid-state NMR spectroscopy of membrane nanotubes, Biochim. Biophys. Acta 1768 (2007) 2026–2029.
[48] F. Re, S. Sesana, A. Barbiroli, F. Bonomi, E. Cazzaniga, E. Lonati, A. Bulbarelli, M. Masserini, Prion protein structure is affected by pH-dependent interaction with membranes: a study in a model system, FEBS Lett. 582 (2008) 215–220.

The fusing ability of sperm is bestowed by CD9-containing vesicles released from eggs in mice

Kenji Miyado*†‡§, Keiichi Yoshida‡¶, Kazuo Yamagata‖, Keiichi Sakakibara*, Masaru Okabe**, Xiaobiao Wang*, Kiyoko Miyamoto*, Hidenori Akutsu*, Takahiko Kondo*, Yuji Takahashi*, Tadanobu Ban††, Chizuru Ito¶, Kiyotaka Toshimori¶, Akihiro Nakamura*, Masahiko Ito*, Mami Miyado*, Eisuke Mekada**, and Akihiro Umezawa*

*National Center for Child Health and Development, 2-10-1 Okura, Setagaya, Tokyo 157-8535, Japan; †School of Biomedical Science, Tokyo Medical and Dental University, Yushima, Bunkyo, Tokyo 113-8510, Japan; ¶Graduate School of Medicine, Chiba University, 1-8-1 Inohana, Chuo-ku, Chiba 260-8670, Japan; ‖Center for Developmental Biology, RIKEN Kobe Institute, 2-2-3 Minatojima-minamimachi, Chuo-ku, Kobe, Hyogo 650-0047, Japan; and **Research Institute for Microbial Diseases, and ††Faculty of Medicine, Osaka University, 3-1 Yamadaoka, Suita, Osaka 565-0871, Japan

Edited by Ryuzo Yanagimachi, University of Hawaii, Honolulu, HI, and approved July 8, 2008 (received for review November 8, 2007)

Membrane fusion is an essential step in the encounter of two nuclei from sex cells—sperm and egg—in fertilization. However, aside from the involvement of two molecules, CD9 and Izumo, the mechanism of fusion remains unclear. Here, we show that sperm–egg fusion is mediated by vesicles containing CD9 that are released from the egg and interact with sperm. We demonstrate that the CD9$^{-/-}$ eggs, which have a defective sperm-fusing ability, have impaired release of CD9-containing vesicles. We investigate the fusion-facilitating activity of CD9-containing vesicles by examining the fusion of sperm to CD9$^{-/-}$ eggs with the aid of exogenous CD9-containing vesicles. Moreover, we show, by examining the fusion of sperm to CD9$^{-/-}$ eggs, that hamster eggs have a similar fusing ability as mouse eggs. The CD9-containing vesicle release from unfertilized eggs provides insight into the mechanism required for fusion with sperm.

fertilization | membrane fusion | EGFP | exosome

Fertilization is an essential process that naturally produces a cell capable of developing into a new individual. It consists of sequential events, including membrane fusion of sperm and egg (1). Despite the importance of understanding fertilization in controlling human reproduction and preserving endangered species, the molecular basis underlying the fusion remains a mystery, however. Previously, we reported that a tetraspan-membrane protein (tetraspanin), CD9, is expressed on the egg plasma membrane and is required for sperm–egg fusion (2–4). A role of CD9 in other fusion events also has been demonstrated (5). When sperm are added to eggs from CD9$^{-/-}$ females, the sperm bind to the egg plasma membrane normally, but fusion is severely impaired (2–4). Two recent observations suggest that CD9 plays a role in the organization of egg membrane. First, CD9 is transferred from the egg to the fertilizing sperm present in the perivitelline space (PVS) (6), suggesting the involvement of a process similar to trogocytosis, a mechanism of cell-to-cell contact-dependent transfer of membrane fragments (7). Second, CD9 deficiency alters the length and density of microvilli on the egg plasma membrane (8). CD9 is also known to be a component of exosomes, membrane vesicles released from a wide range of cells (9, 10). Despite its relationship to CD9, the involvement of exosome release in sperm–egg fusion remains unknown. In the present study, we analyzed the potential of enhanced green fluorescent protein (EGFP)-tagged CD9 (CD9-EGFP) as a reporter protein to study sperm–egg fusion in living mouse eggs.

Results

To observe the movement of CD9 during sperm–egg fusion, we generated a transgenic mouse line that expressed CD9-EGFP only in eggs (Fig. 1*A*), and converted to the genetic background of CD9$^{-/-}$ mice by mating mice. Western blot analysis using anti-CD9 monoclonal antibody (mAb) revealed that an expected CD9-EGFP with a molecular mass of 51 kDa (CD9 and EGFP contributing to 24 and 27 kDa, respectively) was expressed in the eggs collected from Tg$^+$CD9$^{-/-}$ mice; however, the amount of CD9-EGFP expressed in CD9$^{-/-}$ eggs was estimated to be 10% of that of endogenous CD9 in the CD9$^{+/+}$ eggs (Fig. 1*B*). Despite the small amount of CD9-EGFP expressed in eggs, CD9-EGFP demonstrated the ability to reverse the sterility of CD9$^{-/-}$ females (Fig. 1*C*). The numbers of pups obtained from Tg$^+$CD9$^{-/-}$ females (6.4 ± 0.5) were similar to those from

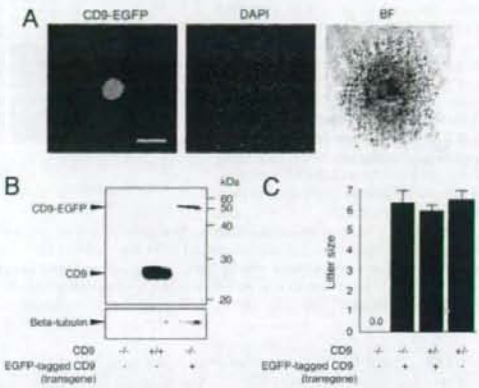

Fig. 1. Generation of mice expressing CD9-EGFP in eggs. (*A*) CD9-EGFP specifically expressed in eggs with mouse ZP3-promoter. Cumulus oocyte complex from Tg$^+$CD9$^{+/+}$ oviducts was collected at 14 h after injection of human chorionic gonadotropin. Nuclei of an egg and cumulus cells were counterstained with DAPI. (*Left*) CD9-EGFP. (*Center*) DAPI. (*Right*) Bright field. Scale bar: 100 μm. (*B*) Western blot analysis for eggs collected from CD9$^{-/-}$, CD9$^{+/+}$, and Tg$^+$CD9$^{-/-}$ mice. The same amounts, including 30 eggs of each lysate, were examined by anti-CD9 and anti-beta-tubulin mAbs (internal control). (*C*) Litter sizes of CD9$^{-/-}$ (n = 31), Tg$^+$CD9$^{-/-}$ (n = 35), Tg$^+$CD9$^{+/+}$ (n = 16), and CD9$^{+/+}$ mice (n = 15) (mean ± SEM). The numbers of females examined are in parentheses.

Author contributions: K. Miyado, K. Yamagata, M.O., and A.U. designed research; K. Miyado, K. Yoshida, K.S., X.W., K. Miyamoto, H.A., T.K., Y.T., T.B., C.I., A.N., M.I., and M.M. performed research; K. Miyado contributed new reagents/analytic tools; K. Miyado, K. Yoshida, H.A., K.T., E.M., and A.U. analyzed data; and K. Miyado wrote the paper.

The authors declare no conflicts of interest.

This article is a PNAS Direct Submission.

Freely available online through the PNAS open access option.

‡K. Miyado and K. Yoshida contributed equally to this work.

§To whom correspondence should be addressed. E-mail: kmiyado@nch.go.jp.

This article contains supporting information online at www.pnas.org/cgi/content/full/0710608105/DCSupplemental.

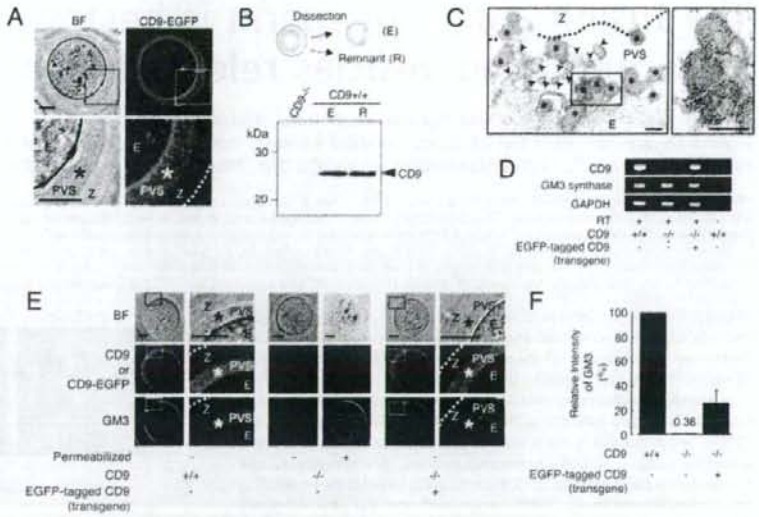

Fig. 2. Identification of secretory vesicles containing CD9 from unfertilized eggs. *A*, A single confocal image showing CD9-EGFP in unfertilized $Tg^+CD9^{-/-}$ eggs (E), including the PVS (*), zona pellucida (Z), and the outer margin of the zona pellucida (dotted line). (*Left*) Bright field. (*Right*) CD9-EGFP. *Lower* are enlarged images of the boxed areas. (*B*) Western blot analysis for eggs mechanically fractionated as shown in the diagram: zona-intact $CD9^{-/-}$ eggs (E) (10 eggs per lane) and zona-free $CD9^{+/+}$ eggs (10 eggs per lane). The medium (R) containing the remnant material from 40 eggs treated with a piezo manipulator was loaded in each lane. (*C*) Immunoelectron-microscopic analysis of $CD9^{+/+}$ eggs. The zona-intact $CD9^{+/+}$ eggs were examined using anti-CD9-mAb and 5-nm gold beads conjugated with anti-rat IgG Ab. Left panel: Image including CD9-containing vesicles (*), microvilli (arrowheads), zona pellucida (Z), perivitelline space (PVS), and egg (E). (*Right*) An enlarged image of the boxed region in the left panel. Scale bar: 200 nm. (*D*) RT-PCR for CD9, GM3 synthase, and glyceraldehyde-3-phosphate dehydrogenase transcripts in $CD9^{+/+}$, $CD9^{-/-}$, and $Tg^+CD9^{-/-}$ eggs. The same amounts, including 50 eggs in each reaction, were examined. The right end lanes are negative controls in which RT was removed from reactions of wild-type eggs. (*E*) Localization of GM3 and CD9 in $CD9^{+/+}$, $CD9^{-/-}$, and $Tg^+CD9^{-/-}$ eggs. (*Left*) Wild-type. (*Middle*) $CD9^{-/-}$. (*Right*) $Tg^+CD9^{-/-}$. Right-side of the sets of wild-type and $Tg^+CD9^{-/-}$ eggs are enlarged images of the boxed regions. The live eggs were examined, and the internal localization of GM3 in $CD9^{-/-}$ eggs was examined under fixed, permeabilized conditions. (*F*) Comparison of the fluorescent intensities of GM3 stained by antibody in wild-type ($n = 10$), $CD9^{-/-}$ ($n = 9$), and $Tg^+CD9^{-/-}$ eggs ($n = 10$) (mean ± SEM). The average values of the wild-type eggs were set to 100%.

$Tg^+CD9^{+/-}$ and $CD9^{+/-}$ females (6.0 ± 0.2 and 6.5 ± 0.5) and greater than those from $CD9^{-/-}$ females (0.0 ± 0.0). The $CD9^{+/-}$ females did not exhibit any loss in fertility that could cause a reduction of litter size relative to that of the $CD9^{+/+}$ females (4). Furthermore, the transgene had no effect on normal fertility. These results demonstrate that transgenically expressed CD9-EGFP can compensate for the loss of intrinsic CD9 and yield eggs with the ability to fuse with sperm.

Based on the foregoing evidence, we observed the subcellular localization of CD9-EGFP in "living" $Tg^+CD9^{-/-}$ eggs (Fig. 2*A*). As expected, confocal microscopic analysis allowed the visualization of two types of CD9-EGFP localization: intense on the plasma membrane and also in the cytoplasm. Unexpectedly, we found loosely filled, noncompacted CD9-EGFP in the PVS, a space formed between the zona pellucida and the plasma membrane of the egg. The localization of CD9 outside the eggs also was confirmed by Western blot analysis using anti-CD9 mAb (Fig. 2*B*). As shown in the diagram, $CD9^{+/+}$ eggs were mechanically fractionated into denuded eggs and other components (R) using a piezo manipulator (11). The fraction R, containing the zona pellucida and the components in the PVS, was centrifuged and subjected to Western blot analysis. The amount of CD9 in the remnant material from 40 eggs was found to be densitometrically equal to that of 10 zona-free eggs, demonstrating an estimated relative abundance of CD9 in the remnant of 20% per egg. Subsequently, we performed immunoelectron-microscopic analysis on the $CD9^{+/+}$ eggs. We identified the vesicles bound to gold particles inside the PVS (Fig. 2*C*). The sectioned microvilli contained a branched network of actin filaments, whereas the variously sized vesicles (50–250 nm in diameter) had uniformly dense materials rather than actin filaments. We also compared $CD9^{+/+}$, $Tg^+CD9^{-/-}$, and $CD9^{-/-}$ eggs by electron-microscopic analysis [supporting information (SI) Fig. S1]. The accumulation of vesicles in the PVS in the $Tg^+CD9^{-/-}$ eggs was comparable to that in the $CD9^{+/+}$ eggs, whereas it was not seen in the $CD9^{-/-}$ or germinal vesicle-staged $CD9^{+/+}$ eggs. These results indicate that 20% of the total amount of CD9 is stored as vesicles in the PVS during meiosis.

We next examined the expression of ganglioside GM3, identified as a CD9-associated molecule (12) and a component of exosomes (10), in $CD9^{+/+}$, $CD9^{-/-}$, and $Tg^+CD9^{-/-}$ eggs. First, we confirmed the expression of GM3 synthase (ST3GalV/SAT-1) (13) in these eggs by RT-PCR (Fig. 2*D*). Then we investigated the localization of GM3 by immunostaining these live eggs with anti-GM3 mAb (Fig. 2*E*). This antibody has been demonstrated to recognize GM3 in the plasma membrane of cells without treatment for permeabilization (14). Finally, we measured the fluorescent intensities of GM3 in these live eggs (Fig. 2*F*). As expected, in wild-type eggs, GM3 was colocalized with CD9 in the PVS and plasma membrane (Fig. 2*E Left* and Fig. 2*F*). In contrast, in $CD9^{-/-}$ eggs, the fluorescent intensities of GM3 were decreased dramatically in the PVS and plasma membrane (0.4% ± 0.2%, relative to 100% for the $CD9^{+/+}$ eggs), consistent with the loss of CD9 (Fig. 2*E Center* and Fig. 2*F*), whereas GM3 could be detected in the cytoplasm of $CD9^{-/-}$ eggs that had been permeabilized by a detergent after fixation. Moreover, the expression of CD9-EGFP reversed the decrease of GM3 in the PVS and plasma membrane of $CD9^{-/-}$ eggs (25.6 ± 10.7%) (Fig. 2*E Right* and Fig. 2*F*), corresponding to the amount of CD9-EGFP quantified by Western blot analysis (Fig. 1*B*). In addition, electron-microscopic analysis revealed that the number of characteristic membrane structures, termed microvilli (1), were significantly decreased in the $CD9^{-/-}$ eggs compared with the $CD9^{+/+}$ eggs (Fig. S2 *A* and *B*). The numbers of microvilli were increased by ≈50% by the expression of CD9-EGFP in the $CD9^{-/-}$ eggs. The analyses of three types of eggs indicate that CD9- and GM3-containing vesicle release is linked to microvilli formation.

We next investigated the involvement of CD9-containing vesicles in sperm–egg fusion (Fig. 3). We found that, based on the length of microvilli (Fig. S2*C*), zona-intact $Tg^+CD9^{-/-}$ eggs can be categorized into two groups (Fig. 3*A*). From single

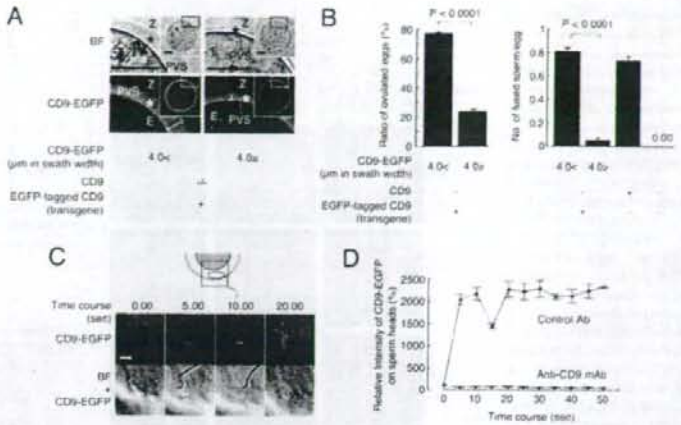

Fig. 3. Involvement of CD9-containing vesicles in sperm–egg fusion. (*A*) Categorization of $Tg^+CD9^{-/-}$ eggs (E) into two groups according to the thickness of CD9-EGFP in the PVS (*) and the inner region of the zona pellucida (Z) (≤4.0 μm or ≤ 4.0 μm), indicated by double-headed lines. The boxed regions in *Insets* are enlarged. Scale bar: 20 μm. (*B*) Comparison of the fusing ability of two groups of $Tg^+CD9^{-/-}$ eggs with wild-type sperm. Left graph: Ratio of two groups of $Tg^+CD9^{-/-}$ eggs ovulated from 12 females (mean ± SEM). Right graph: Number of sperm fused per egg in two groups of zona-intact $Tg^+CD9^{-/-}$ eggs ovulated from 12 females (≤4.0 μm, $n = 204$; >4.0 μm, $n = 66$) (mean ± SEM). $CD9^{+/+}$ ($n = 120$) and $CD9^{-/-}$ ($n = 112$) served as positive and negative controls, respectively. (*C* and *D*) Monitoring of the association of egg CD9-containing vesicles with wild-type sperm. $Tg^+CD9^{-/-}$ eggs were incubated with the sperm and monitored immediately after the sperm penetrated the zona pellucida under the presence of anti-CD9 mAb (boxed region). The values were calculated from data scanning by confocal microscopy (15 sperm in triplicate dishes) Blue: Preimmune rat IgG. Red: Anti-CD9 mAb (KMC8) (mean ± SEM). The average values of the fluorescent intensities of CD9-EGFP at 0 s were set to 100%, and the final concentration of antibodies was adjusted to 50 μg/ml. Scale bar, 5 μm.

confocal images sectioned through the largest diameter, the accumulation of CD9-EGFP from the plasma membrane to the inner region of the zona pellucida was >4.0 μm in swath width in one group and ≤ 4.0 μm in the other group. The accumulation of CD9-EGFP was predicted to show that CD9-containing vesicles are more highly accumulated within the PVS in the >4.0-μm group compared with the ≤ 4.0-μm group. Comparing the ratio of these two groups in $Tg^+CD9^{-/-}$-ovulated eggs revealed a much higher percentage of the >4.0-μm group (77.0 ± 1.3% vs.23.7 ± 1.5%) (Fig. 3*B Left*). Therefore, we focused on the heterogeneity of CD9-EGFP accumulation within the PVS and determined the ratio of the two groups in zona-intact $Tg^+CD9^{-/-}$ eggs that successfully fused with the sperm 6 h after insemination. The >4.0-μm group of $Tg^+CD9^{-/-}$ eggs showed higher activity for fusion with sperm (0.81 ± 0.04 sperm fused per egg), compared with the ≤40-μm group of $Tg^+CD9^{-/-}$ eggs (0.05 ± 0.03) and the $CD9^{-/-}$ eggs (0.00 ± 0.00), and comparable activity to that of wild-type eggs (0.73 ± 0.04) (Fig. 3*B Right*). The average activity of all $Tg^+CD9^{-/-}$ eggs (0.72 ± 0.03 sperm fused per egg) was equal to that of wild-type eggs (0.73 ± 0.04 sperm fused per egg). The difference between the two groups of $Tg^+CD9^{-/-}$ eggs was statistically significant (Fig. 3*B*). These results suggest that the quantities of CD9-containing vesicles, as assessed by the swath width of CD9-EGFP, are strongly correlated with the frequency of sperm–egg fusion.

To detect the association between sperm and CD9-containing vesicles, we serially monitored the wild-type sperm that penetrated the zona pellucida of the $Tg^+CD9^{-/-}$ eggs (Fig. 3 *C* and *D*). As shown in the diagram, we began monitoring the sperm immediately after the head portion of sperm penetrated the zona pellucida of the $Tg^+CD9^{-/-}$ eggs (Fig. 3*C Upper*, boxed area in the diagram). Soon after we began to monitor the sperm, the fluorescent intensities of CD9-EGFP on the sperm heads increased and then decreased rapidly between 0 s and 15 s, then increased again, reaching a maximum at 20 s. At this point, the CD9-EGFP fully covered the surface of the sperm heads. In contrast, when the sperm were incubated with $Tg^+CD9^{-/-}$ eggs in the medium containing anti-CD9 mAb, no increase in intensity of CD9-EGFP on the sperm heads was detected. Anti-CD9 mAbs have been reported to inhibit sperm–egg fusion (4, 15, 16). Our findings demonstrate that the anti-CD9 mAb inhibited the association of sperm with CD9-containing vesicles in parallel to inhibition of sperm–egg fusion.

To determine whether CD9-containing vesicles are capable of initiating sperm–egg fusion, we incubated the sperm with $CD9^{-/-}$ eggs in medium containing the vesicles collected from $CD9^{+/+}$ eggs (Fig. 4 and Fig. S3). To restrict the source of CD9 into the vesicles from the $CD9^{+/+}$ eggs, we used sperm collected from the epididymis of $CD9^{-/-}$ males. We estimated the capability of the vesicles to influence fusion by counting the number of sperm fused with $CD9^{-/-}$ eggs. As shown in the experimental design, after the zona pellucida was removed from the $CD9^{-/-}$ eggs, the eggs were incubated with sperm in the medium containing the vesicles (Fig. 4*A*). When examined at 1 h after incubation, the sperm were seen to be capable of fusing with $CD9^{-/-}$ eggs after co-incubation with the vesicles (Fig. 4*A Center*), indicating restoration of the fusibility of $CD9^{-/-}$ eggs with the sperm (0.58 ± 0.07 sperm fused per egg) (Fig. 4*B*). We detected further evidence of sperm–egg fusion in the $CD9^{-/-}$ eggs from which a second polar body had been extruded. In contrast, we did not detect improved fusibility of sperm with eggs in medium depleted of CD9-containing vesicles using beads conjugated with anti-CD9 mAb (Fig. 4*A Right* and *B*). After treatment with the beads, the quantity of CD9 in the depleted medium was significantly decreased, to 16% of the untreated medium (Fig. 4*C*). In addition, $CD9^{-/-}$ remnants failed to rescue the fusing ability of $CD9^{-/-}$ eggs. These findings indicate that the association with CD9-containing vesicles renders the sperm capable of fusing with eggs without endogenous CD9 expression. We estimated the relative abundance of CD9 in the remnant as 18% of the total amount in the eggs (Fig. 4*C*). We further found

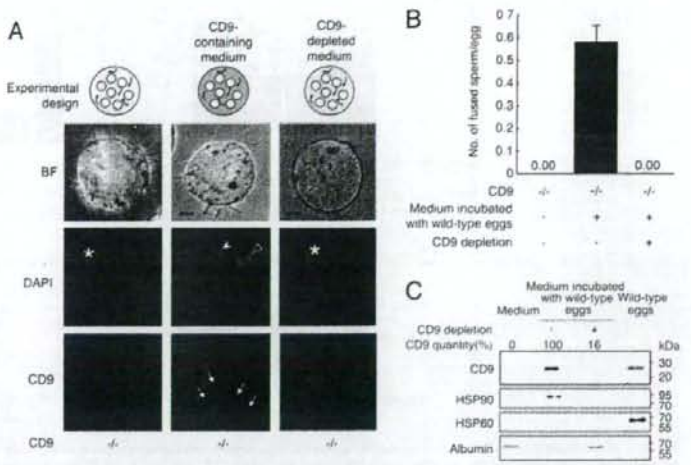

Fig. 4. Identification of fusion-facilitating activity of CD9-containing vesicles. (*A*) Estimation of the fusion-facilitating ability of the vesicles in sperm–egg fusion. As shown in the experimental design, $CD9^{-/-}$ sperm were incubated with $CD9^{+/+}$ eggs (white circles) in media containing egg-released vesicles after the zona pellucida was removed from these eggs. CD9 was detected by anti-CD9 mAb conjugated with Alexa488. The eggs were preloaded with DAPI before incubation with the sperm, to allow counting of the number of fused sperm. (*Left*) $CD9^{+/+}$ eggs at 1 h after incubation with the sperm, as a negative control. *Center* $CD9^{-/-}$ eggs cultured in the medium containing CD9 collected from wild-type eggs. (*Right*) $CD9^{-/-}$ eggs cultured in the medium depleted of CD9 by beads conjugated with anti-CD9 mAb, showing the fused sperm to eggs (arrowhead), metaphase II–arrested chromosomes (*), a second polar body (open arrowhead), and CD9 translocated on the sperm heads (arrow). The fluorescent z-series images were projected as three-dimensional images. Scale bar: 20 μm. (*B*) Number of fused sperm with the zona-free eggs counted at 1 h after incubation (mean ± SEM): $CD9^{+/+}$ eggs as a negative control (n = 51), $CD9^{-/-}$ eggs cultured in the medium containing CD9 (n = 112), and $CD9^{-/-}$ eggs cultured in the medium depleted of CD9 by antibody-conjugated beads (n = 74). The total numbers of eggs examined are in parentheses. (*C*) Western blot analysis of the media incubated with $CD9^{+/+}$ eggs for CD9, HSP90, and HSP60. Loaded samples (left to right): The medium as a negative control, the medium containing the remnant material from 40 eggs per lane (bead-untreated and -treated), and 5 eggs per lane as a positive control. The albumin contained in the medium was detected by Coomassie brilliant blue staining as an internal control. The quantities of CD9 in the media were measured densitometrically (using National Institutes of Health Image software).

that the decreased amount of CD9 after the bead treatment was synchronized with that of a cytoplasmic chaperone, HSP90 (17), but not with a mitochondrial chaperone, HSP60 (18). Our analysis of the egg-conditioned medium indicated that CD9-containing vesicles contained HSP90, a conserved component of exosomes (9, 10).

To estimate the contribution of CD9-containing vesicles to sperm–egg fusion, we examined the restoration of the impaired sperm-fusing ability in $CD9^{-/-}$ eggs co-incubated with $CD9^{+/-}$ or $CD9^{+/+}$ eggs expressing endogenous CD9 (Figs. 5 and S4*A*). We predicted that when sperm were incubated with a mixture of eggs, the vesicles released from $CD9^{+/-}$ or $CD9^{+/+}$ eggs would

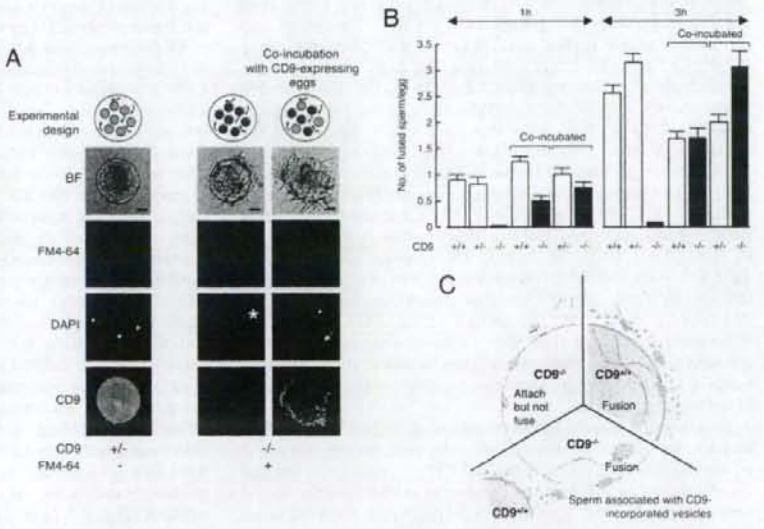

Fig. 5. Recovery of impaired fusion of $CD9^{-/-}$ eggs with sperm by CD9-containing vesicles. (*A*) Estimation of the fusion-facilitating ability of the vesicles in sperm–egg fusion. As shown in the experimental design, sperm were incubated with a mixture of CD9-expressing eggs (green circles) and $CD9^{-/-}$ eggs (red circles) after the zona pellucida was removed from these eggs. The eggs were preloaded with DAPI before incubation with sperm, to allow counting of the number of fused sperm. $CD9^{-/-}$ eggs were prestained with FM4–64 and thus were easily distinguished from CD9-expressing eggs after incubation with the sperm. (*Left*) $CD9^{+/+}$ eggs at 1 h after incubation with the sperm, as a positive control. (*Center*) $CD9^{-/-}$ eggs, as a negative control. (*Right*) $CD9^{-/-}$ eggs co-incubated with $CD9^{+/+}$ eggs, showing fused sperm to egg (arrowheads), metaphase II–arrested chromosomes (*), and extruded second polar body (arrow). The fluorescent z-series images were projected as three-dimensional images. CD9 was detected by anti-CD9 mAb conjugated with Alexa488. Scale bar: 20 μm. (*B*) Numbers of fused sperm with the zona-free eggs counted at 1 and 3 h after incubation (mean ± SEM). $CD9^{+/+}$ (1 h: n = 34; 3 h: n = 55), $CD9^{+/-}$ (1 h: n = 71; 3 h: n = 79), and $CD9^{-/-}$ eggs (1 h: n = 100; 3 h: n = 115) were separately incubated with sperm. Total number of coincubated eggs examined: $CD9^{+/+}$ eggs (n = 54) coincubated with $CD9^{-/-}$ eggs (n = 60), and $CD9^{+/+}$ eggs (n = 65) coincubated with $CD9^{-/-}$ eggs (n = 74) at 1 h; $CD9^{+/-}$ eggs (n = 51) coincubated with $CD9^{-/-}$ eggs (n = 33), and $CD9^{+/+}$ eggs (n = 98) coincubated with $CD9^{-/-}$ eggs (n = 90) at 3 h. (*C*) Schematic model of involvement of CD9-containing vesicles in sperm–egg fusion: $CD9^{+/-}$ (green), $CD9^{-/-}$ (light blue), and $CD9^{-/-}$ eggs coincubated with $CD9^{+/+}$ wild-type eggs with sperm (yellow).

interact with sperm, and these sperm could fuse with $CD9^{-/-}$ eggs. If sperm-fusing ability were regulated mainly by CD9-containing vesicles, then the number of sperm fused to $CD9^{-/-}$ eggs would be predicted to be almost equal to that fused to $CD9^{+/+}$ or $CD9^{+/-}$ eggs coincubated with $CD9^{-/-}$ eggs. We counted the number of fused sperm in coincubated CD9-expressing eggs ($CD9^{+/-}$ and $CD9^{+/+}$) and $CD9^{-/-}$ eggs. The $CD9^{-/-}$ eggs were prestained with FM4–64 (19), a fluorescent dye used to stain the membrane of live cells, and thus could be easily distinguished from the $CD9^{+/-}$ and $CD9^{+/+}$ eggs. FM4–64 did not transfer between the $CD9^{-/-}$ eggs and the $CD9^{+/-}$ or $CD9^{+/+}$ eggs. As shown in the experimental design, after the zona pellucida was removed from the eggs, $CD9^{-/-}$ eggs (red circles) were mixed with $CD9^{+/-}$ or $CD9^{+/+}$ eggs (green circles), and sperm were added to the medium containing these eggs (Fig. 5*A*). At 1 h after insemination, significant fusion of sperm with the $CD9^{-/-}$ eggs was facilitated (0.75 ± 0.11 and 0.50 ± 0.09 sperm fused per egg), corresponding to that in the $CD9^{+/-}$ (1.00 ± 0.13) and $CD9^{+/+}$ eggs (1.25 ± 0.10). At 3 h after insemination, the fusion of sperm with the $CD9^{-/-}$ eggs was restored (3.06 ± 0.30 and 1.70 ± 0.18 sperm fused per egg) to levels comparable to those in the $CD9^{+/-}$ (2.00 ± 0.15) and $CD9^{+/+}$ eggs (1.69 ± 0.13). We also detected a second polar body extruding from the $CD9^{-/-}$ eggs (Fig. 5*A Right*, arrow). In contrast, we did not observe the translocation of vesicles from the $CD9^{+/-}$ and $CD9^{+/+}$ eggs to the $CD9^{-/-}$ eggs when sperm were not added to the mixture, even after 10 h of incubation (Fig. S4*B*). These data demonstrate that the defect in the fusing ability of $CD9^{-/-}$ eggs is caused by dysfunction of the mechanism facilitating the sperm-fusing activity through CD9-containing vesicles.

To further study the involvement of CD9-containing vesicles in regulating sperm-fusing ability, we evaluated the capability of hamster eggs in sperm–egg fusion (Fig. S5). Hamster eggs have the ability to fuse with other mammalian sperm and thus are used as a tool to evaluate the fusing ability of human sperm (20). When hamster eggs were incubated with $CD9^{-/-}$ eggs after the zona pellucida was removed from these eggs, the sperm-fusing ability of these eggs was improved significantly. The sperm-fusing ability acquired through the exposure to hamster eggs was not as great as that produced by exposure to mouse eggs, probably due to the slightly different CD9 in hamster and mouse eggs (21). These results indicate that the function of CD9-containing vesicles in the acquisition of sperm-fusing ability is widely conserved in mammals.

Discussion

In sperm–egg fusion, there is a significant direct interaction between the cell membranes of sperm and eggs (1, 20, 22); however, our results demonstrate that CD9-containing vesicle–sperm interaction precedes the direct cell membrane interaction between sperm and eggs. Based on our data, we propose that the release of CD9-containing vesicles from eggs before fertilization facilitates the sperm-fusing ability that renders the sperm competent to fuse with $CD9^{-/-}$ eggs (Fig. 5*C*). Our finding of CD9-EGFP in living unfertilized eggs demonstrates that CD9-containing vesicles are present in the PVS, and that these vesicles accumulate inside the PVS during the germinal vesicle (1) and metaphase II-arrested stages (1). During this period, the egg undergoes drastic cytological changes with the increased number of microvilli (1, 22), predicting the correlation between vesicle release and microvilli formation. As expected, this correlation is supported by the finding that CD9 deficiency leads not only to impaired microvilli formation (8) (Fig. S2), but also to decreased accumulation of vesicles within the PVS. These data support the association between the release of CD9-containing vesicles from eggs and the formation of microvilli on the egg plasma membrane.

As reported previously, somatic cells are capable of releasing proteins and lipids included in membrane organelles, termed exosomes (9, 10), which are pinched out from the plasma membrane (23). Exosomes share many additional properties with retroviral particles, including similar lipid and protein compositions, such as tetraspanin (23). GM3 and HSP90 are known to be conserved components of exosomes (10). Our results show that CD9-containing vesicles released from eggs share these two components, implying that the vesicles are "exosome-like." Previous studies of macrophages have proposed that exosome biogenesis occurs only by outward budding at endosomal membranes, followed by the fusion of vesicle-laden endosomes with the plasma membrane (9, 23). If the CD9-containing vesicle were derived from exosomes and generated from the fusion of endosomes with the plasma membrane, then the vesicles would contain some proteases (9, 23), fuse with the sperm membrane, and possibly activate the sperm fusogenic factor(s) by enzymatic activities.

In hamster eggs, expansion of the PVS has been deemed essential or at least beneficial to normal fertilization (20, 21, 24), indicating that materials involved in fusion with sperm are released from eggs before fertilization in hamsters and in mice. Because anti-CD9 mAbs are not available for hamster CD9, we could not directly confirm CD9-containing vesicle release from hamster eggs before fertilization. Instead, our co-incubation assay demonstrated that hamster eggs facilitate the fusion of sperm with $CD9^{-/-}$ eggs, indicating that hamster eggs share a similar mechanism with mouse eggs through egg-released materials. Moreover, it has been reported that growing oocytes bind to sperm and transfer fluorescent dyes to the sperm head (25). At this stage, oocytes have CD9 on the cell membrane but lack CD9-containing vesicles (Fig. S1). We presume that the transfer of fluorescent dye from growing oocytes to sperm heads is mediated by CD9 on the cell membrane. Based on our findings, we propose that the CD9-containing vesicle has an ability to facilitate sperm—egg fusion. This knowledge has great potential for clinical applications, such as the induction of sperm–egg fusion using exogenous sources.

Materials and Methods

Animals. The mice that we produced were back-crossed into a C57BL/6 genetic background. Wild-type eggs were collected from C57BL/6 females (8–12 weeks old). Wild-type sperm were obtained from the epididymides of B6C3F1 males (8–12 weeks old). Hamster eggs were obtained commercially as frozen unfertilized eggs (NOSAN).

Antibodies and Chemicals. Antibodies against CD9 (KMC; BD PharMingen), beta-tubulin (Tub2.1; Sigma), HSP60 (24/HSP60; BD PharMingen), HSP90 (16F1; MBL), and GM3 (GMR6; Seikagaku) were used. Antibodies labeled with biotin by a labeling kit (Dojindo) and horseradish peroxidase-conjugated streptavidin (Sigma) were used for Western blot analysis. For immunostaining, antibodies were labeled directly with Alexa488 and Alexa546 using labeling kits (Invitrogen). FM4–64 (Invitrogen) was used to define the lipid bilayer of live eggs without disturbing sperm–egg fusion (10 μM at final concentration). We used DAPI (Invitrogen), a fluorescent dye that slowly permeates the living cell membrane (semipermeable) and slowly leaks out of cells after washing relative to Hoechst33342 (permeable), in counting the number of sperm fused per egg.

Transgenic Mice. The construct expressing mouse CD9 tagged at the N terminus with EGFP (CD9-EGFP) was subcloned into plasmid DNA-containing mouse ZP3 promoter (26). The expression cassette was excised by restriction enzyme digestion and microinjected into fertilized eggs of C57BL/6 mice, according to standard techniques (27).

Genotyping and RT-PCR. Mouse genotyping and RT-PCR were performed following standard procedures (27). (Primer sets are listed in Table S1).

Egg Collection. Eggs were collected from the oviduct 14–16 h after human chorionic gonadotropin injection (4). The eggs were placed in a drop of TYH

medium (28). Sperm collected from the epididymides were capacitated in a 100-μl drop of medium. The eggs were incubated with 1.5 – 10^5 sperm/ml at 37°C in 5% CO_2, and unbound sperm were washed away. The zona pellucida was removed from the eggs with acidic Tyrode's solution (4) or a piezo manipulator (11). A hole was punched through the zona pellucida with a piezo manipulator, and the eggs were removed. All materials were aspirated, including the medium but not the eggs, and used as "remnants."

Immunostaining. Zona-intact live eggs were stained with diluted antibodies in TYH medium for 30 min at 37°C, and the nonspecifically accumulated antibodies in the PVS were washed away after a brief incubation (30 min) in the medium. To measure the fluorescent intensities of GM3, three types of eggs were stained by Alexa546-labeled anti-GM3 mAb in TYH medium for 30 min, then washed in the medium for 30 min. Staining was visualized using a laser scanning confocal microscope (LSM 510 META; Carl Zeiss).

Electron-Microscopic Analysis. Live eggs were incubated with anti-CD9 mAb and anti-rat IgG mAb tagged with 5-nm gold beads. After incubation, the eggs were fixed by glutaraldehyde and osmic acid solutions. Ultra-thin sections were prepared as described in ref. 29. Eggs denuded with acid Tyrode's solution were fixed with a mixture of paraformaldehyde and glutaraldehyde and osmic acid solutions.

***In Vitro* Fertilization.** To observe the fusion with the sperm, zona-intact and zona-free eggs were incubated with DAPI (10 μg/ml) in the medium for 20 min, then washed before the sperm were added. This procedure allowed the staining of only fused sperm nuclei by dye-transfer into sperm after membrane fusion. At 1 h or 3 h after incubation in a 30-μl drop of medium, the eggs were fixed with a mixture of paraformaldehyde and glutaraldehyde for 20 min at 4°C.

Monitoring the Association of CD9-Containing Vesicles with Sperm. Eggs collected from Tg $^+$CD9$^{-/-}$ females were set in a 30-μl drop of TYM medium. The sperm were added to the eggs at a final concentration of 1.5 – 10^5/ml after incubation in the medium for 2 h. Posts of latex beads were deposited around the eggs. A glass coverslip was carefully pressed down onto the posts until the egg were fixed. The medium containing eggs and sperm was cooled to 10°C before observation. Cooling reduced the sperm motility. This procedure allowed us to measure the CD9-EGFP fluorescence on the sperm head using a confocal microscope. Images of the sperm were captured at 1 frame/s. The average value of the fluorescent intensities of CD9-EGFP at 0 s was set to 100%, and the final concentration of antibodies was adjusted to 50 μg/ml. The data are measurements of serial images from 15 wild-type sperm in triplicate dishes.

Collection of CD9-Containing Vesicles. The medium containing the vesicles was collected from denuded wild-type eggs. The eggs were cultured in a 60-μl drop of medium for 2 h after the zona pellucida was removed from the eggs. Collecting the medium containing the vesicles required an incubation time of 2 h. The collected medium was used for analysis of vesicle components and evaluation of sperm-fusing ability. CD9-depleted medium was used as a negative control. After the zona pellucida was removed from CD9$^{-/-}$ eggs, the eggs were incubated with the sperm in the medium containing CD9-incorporated vesicles for 1 h, for comparison with the vesicle-depleted medium. Details are shown in Fig. S3.

Western Blot Analysis. Quantities of proteins were examined by Western blot analysis, as described in ref. 4. As an internal loading control, quantities of albumin included in the medium were examined using Coomassie brilliant blue staining. Details are shown in Fig. S3.

Coincubation of Two Types of Eggs. CD9$^{-/-}$ eggs and CD9-expressing eggs (CD9$^{+/-}$ and CD9$^{+/+}$) were incubated in each 30-μl drop of medium after the zona pellucida was removed from these eggs. At 2 h after incubation, the CD9$^{-/-}$ eggs were added into the cultured medium of the CD9-expressing eggs. Sperm were added into the medium containing two types of eggs and incubated for 1 or 3 h. Details are shown in Fig. S4A. The frozen hamster eggs also were incubated with the CD9$^{-/-}$ eggs and wild-type sperm for 1 h. The zona pellucida of frozen hamster eggs was hardened, and removing the zona pellucida using acid Tyrode's solution took 5 min. Details are shown in Fig. S5A.

ACKNOWLEDGMENTS. This work was supported by a Precursory Research for Embryonic Science and Technology (PRESTO) grant from the Japanese Ministry of Health, Labor and Welfare and by a Grant-in-Aid for Scientific Research from the Japanese Ministry of Education, Culture, Sports, and Technology.

1. Yanagimachi R (1994) in *The Physiology of Reproduction*, eds Knobil E, Neill JD (Raven, New York), pp 189–317.
2. Kaji K, *et al.* (2000) The gamete fusion process is defective in eggs of Cd9-deficient mice. *Nat Genet* 24:279–282.
3. Le Naour F, Rubinstein E, Jasmin C, Prenant M, Boucheix C (2000) Severely reduced female fertility in CD9-deficient mice. *Science* 287:319–321.
4. Miyado K, *et al.* (2000) Requirement of CD9 on the egg plasma membrane for fertilization. *Science* 287:321–324.
5. Hemler ME (2003) Tetraspanin proteins mediate cellular penetration, invasion, and fusion events and define a novel type of membrane microdomain. *Annu Rev Cell Dev Biol* 19:397–422.
6. Barraud-Lange V, Naud-Barriant N, Bomsel M, Wolf J-P, Ziyyat A (2007) Transfer of oocyte membrane fragments to fertilizing spermatozoa. *FASEB J* 21:3446–3449.
7. Joly E, Hudrisier D (2003) What is trogocytosis and what is its purpose? *Nat Immunol* 4:815.
8. Runge K-E, *et al.* (2007) Oocyte CD9 is enriched on the microvillar membrane and required for normal microvillar shape and distribution. *Dev Biol* 304:317–325.
9. Trajkovic K, *et al.* (2008) Ceramide triggers budding of exosome vesicles into multivesicular endosomes. *Science* 319:1244–1247.
10. Wubbolts R, *et al.* (2003) Proteomic and biochemical analyses of human B cell-derived exosomes: Potential implications for their function and multivesicular body formation. *J Biol Chem* 278:10963–10972.
11. Yamagata K, *et al.* (2002) Sperm from the calmegin-deficient mouse have normal abilities for binding and fusion to the egg plasma membrane. *Dev Biol* 250:348–357.
12. Mitsuzuka K, Handa K, Satoh M, Arai Y, Hakomori S (2005) A specific microdomain ("glycosynapse 3") controls phenotypic conversion and reversion of bladder cancer cells through GM3-mediated interaction of alpha3beta1 integrin with CD9. *J Biol Chem* 280:35545–35553.
13. Yamashita T, *et al.* (2003) Enhanced insulin sensitivity in mice lacking ganglioside GM3. *Proc Natl Acad Sci USA* 100:3445–3449.
14. Kotani M, Ozawa H, Kawashima I, Ando S, Tai T (1992) Generation of one set of monoclonal antibodies specific for a-pathway ganglio-series gangliosides. *Biochim Biophys Acta* 1117:97–103.
15. Chen MS, *et al.* (1999) Role of the integrin-associated protein CD9 in binding between sperm ADAM 2 and the egg integrin alpha6beta1: Implications for murine fertilization. *Proc Natl Acad Sci USA* 96:11830–11835.
16. Miller B-J, Georges-Labouesse E, Primakoff P, Myles D-G (2000) Normal fertilization occurs with eggs lacking the integrin alpha6beta1 and is CD9-dependent. *J Cell Biol* 149:1289–1296.
17. Callahan M-K, Garg M, Srivastava P-K (2008) Heat-shock protein 90 associates with N-terminal extended peptides and is required for direct and indirect antigen presentation. *Proc Natl Acad Sci USA* 105:1662–1667.
18. Cheng M-Y, Hartl F-U, Horwich A-L (1990) The mitochondrial chaperonin hsp60 is required for its own assembly. *Nature* 348:455–458.
19. Bolte S, *et al.* (2004) FM-dyes as experimental probes for dissecting vesicle trafficking in living plant cells. *J Microsc* 214:159–173.
20. Yanagimachi R, Yanagimachi H, Rogers B-J (1976) The use of zona-free animal ova as a test system for the assessment of the fertilizing capacity of human spermatozoa. *Biol Reprod* 15:471–476.
21. Ponce R-H, Yanagimachi R, Urch U-A, Yamagata T, Ito M (1993) Retention of hamster oolemma fusibility with spermatozoa after various enzyme treatments: A search for the molecules involved in sperm–egg fusion. *Zygote* 1:163–171.
22. Primakoff P, Myles D-G (2002) Penetration, adhesion, and fusion in mammalian sperm–egg interaction. *Science* 296:2183–2185.
23. Booth A-M, *et al.* (2006) Exosomes and HIV Gag bud from endosome-like domains of the T cell plasma membrane. *J Cell Biol* 172:923–935.
24. Okada A, Yanagimachi R, Yanagimachi H (1986) Development of a cortical granule-free area of cortex and the perivitelline space in the hamster oocyte during maturation and following ovulation. *J Submicrosc Cytol* 18:233–247.
25. Zuccotti M, Yanagimachi R, Yanagimachi H (1991) The ability of hamster oolemma to fuse with spermatozoa: Its acquisition during oogenesis and loss after fertilization. *Development* 112:143–152.
26. Rankin T-L, *et al.* (1998) Human ZP3 restores fertility in Zp3 null mice without affecting order-specific sperm binding. *Development* 125:2415–2424.
27. Hogan B, Costantini F, Lacy E (1986) in *Manipulating the Mouse Embryo* (Cold Spring Harbor Lab Press, Cold Spring Harbor, NY), pp 217–252.
28. Toyoda Y, Chang M-C (1974) Capacitation of epididymal spermatozoa in a medium with high K-Na ratio and cyclic AMP for the fertilization of rat eggs in vitro. *J Reprod Fertil* 36:125–134.
29. Toshimori K, Saxena D-K, Tanii I, Yoshinaga K (1998) An MN9 antigenic molecule, equatorin, is required for successful sperm–oocyte fusion in mice. *Biol Reprod* 59:22–29.

doi:10.1038/nature07027

LETTERS

IGFBP-4 is an inhibitor of canonical Wnt signalling required for cardiogenesis

Weidong Zhu[1]*, Ichiro Shiojima[1]*, Yuzuru Ito[2]*, Zhi Li[1], Hiroyuki Ikeda[1], Masashi Yoshida[1], Atsuhiko T. Naito[1], Jun-ichiro Nishi[1], Hiroo Ueno[3], Akihiro Umezawa[4], Tohru Minamino[1], Toshio Nagai[1], Akira Kikuchi[5], Makoto Asashima[2,6,7] & Issei Komuro[1]

Insulin-like growth-factor-binding proteins (IGFBPs) bind to and modulate the actions of insulin-like growth factors (IGFs)[1]. Although some of the actions of IGFBPs have been reported to be independent of IGFs, the precise mechanisms of IGF-independent actions of IGFBPs are largely unknown[1,2]. Here we report a previously unknown function for IGFBP-4 as a cardiogenic growth factor. IGFBP-4 enhanced cardiomyocyte differentiation *in vitro*, and knockdown of *Igfbp4* attenuated cardiomyogenesis both *in vitro* and *in vivo*. The cardiogenic effect of IGFBP-4 was independent of its IGF-binding activity but was mediated by the inhibitory effect on canonical Wnt signalling. IGFBP-4 physically interacted with a Wnt receptor, Frizzled 8 (Frz8), and a Wnt co-receptor, low-density lipoprotein receptor-related protein 6 (LRP6), and inhibited the binding of Wnt3A to Frz8 and LRP6. Although IGF-independent, the cardiogenic effect of IGFBP-4 was attenuated by IGFs through IGFBP-4 sequestration. IGFBP-4 is therefore an inhibitor of the canonical Wnt signalling required for cardiogenesis and provides a molecular link between IGF signalling and Wnt signalling.

The heart is the first organ to form during embryogenesis, and abnormalities in this process result in congenital heart diseases, the most common cause of birth defects in humans[3]. Molecules that mediate cardiogenesis are of particular interest because of their potential use for cardiac regeneration[4,5]. Previous studies have shown that soluble growth factors such as bone morphogenetic proteins (BMPs), fibroblast growth factors (FGFs), Wnts and Wnt inhibitors mediate the tissue interactions that are crucial for cardiomyocyte specification[3,4]. We proposed that there might be additional soluble factors that modulate cardiac development and/or cardiomyocyte differentiation.

P19CL6 cells differentiate into cardiomyocytes with high efficiency in the presence of 1% dimethylsulphoxide (DMSO)[6]. We cultured P19CL6 cells with culture media conditioned by various cell types in the absence of DMSO, and screened the cardiogenic activity of the conditioned media. The extent of cardiomyocyte differentiation was assessed by the immunostaining with MF20 monoclonal antibody that recognizes sarcomeric myosin heavy chain (MHC). Among the several cell types tested, culture media conditioned by a murine stromal cell line OP9 induced cardiomyocyte differentiation of P19CL6 cells without DMSO treatment (Fig. 1a, left and middle panels). Increased MF20-positive area was accompanied by the induction of cardiac marker genes such as *αMHC*, *Nkx2.5* and *GATA-4*, and by the increased protein levels of cardiac troponin T (cTnT) (Fig. 1a, right panel). In contrast, culture media conditioned by COS7 cells, mouse embryonic fibroblasts, NIH3T3 cells, HeLa cells, END2 cells (visceral endoderm-like cells), neonatal rat cardiomyocytes and neonatal rat cardiac fibroblasts did not induce cardiomyocyte differentiation of P19CL6 cells in the absence of DMSO (Fig. 1a and data not shown). From these observations, we postulated that OP9 cells secrete one or more cardiogenic growth factors.

To identify an OP9-derived cardiogenic factor, complementary DNA clones isolated by a signal sequence trap method from an OP9 cell cDNA library[7] were tested for their cardiogenic activities by transient transfection. When available, recombinant proteins were also used to confirm the results. Among candidate factors tested, IGFBP-4 induced cardiomyocyte differentiation of P19CL6 cells, as demonstrated by the increase in MF20-positive area and the induction of cardiac markers (Fig. 1b). We also cultured P19CL6 cells with OP9-conditioned media pretreated with an anti-IGFBP-4 neutralizing antibody. The application of an anti-IGFBP-4 neutralizing antibody attenuated the efficiency of cardiomyocyte differentiation induced by OP9-conditioned media (Fig. 1c). These findings strongly suggest that IGFBP-4 is a cardiogenic factor secreted from OP9 cells.

Because IGFBPs have been characterized as molecules that bind to and modulate the actions of IGFs, we tested whether IGFBP-4 promotes cardiogenesis by either enhancing or inhibiting the actions of IGFs. We first treated P19CL6 cells with a combination of anti-IGF-I and IGF-II-neutralizing antibodies or a neutralizing antibody against type-I IGF receptor. If IGFBP-4 induces cardiomyocyte differentiation by inhibiting IGF signalling, treatment with these antibodies should induce cardiomyocyte differentiation and/or enhance the cardiogenic effects of IGFBP-4. In contrast, if IGFBP-4 promotes cardiogenesis by enhancing IGF signalling, treatment with these antibodies should attenuate IGFBP-4-mediated cardiogenesis. However, treatment with these antibodies did not affect the efficiency of IGFBP-4-induced cardiomyocyte differentiation (Fig. 1d and data not shown). Treatment of P19CL6 cells with IGF-I and IGF-II also did not induce cardiomyocyte differentiation (data not shown). Furthermore, treatment with an IGFBP-4 mutant (IGFBP-4-H74P; His 74 replaced by Pro)[8] that is unable to bind IGFs induced cardiomyocyte differentiation of P19CL6 cells even more efficiently than wild-type IGFBP-4 (Fig. 1e). This is presumably due to the sequestration of wild-type IGFBP-4 but not mutant IGFBP-4-H74P by endogenous IGFs. In agreement with this idea, exogenous IGFs attenuated wild-type IGFBP-4-induced but not IGFBP-4-H74P-induced cardiogenesis (Fig. 1f). Taken together, these observations indicate

[1]Department of Cardiovascular Science and Medicine, Chiba University Graduate School of Medicine, Chiba 260-8670, Japan. [2]ICORP Organ Regeneration Project, Japan Science and Technology Agency (JST), Tokyo 153-8902, Japan. [3]Institute of Stem Cell Biology and Regenerative Medicine, Stanford University School of Medicine, Stanford, California 94305, USA. [4]Department of Reproductive Biology, National Institute for Child Health and Development, Tokyo 157-8535, Japan. [5]Department of Biochemistry, Graduate School of Biomedical Sciences, Hiroshima University, Hiroshima 734-8551, Japan. [6]Department of Life Sciences (Biology), Graduate School of Arts and Science, The University of Tokyo, Tokyo 153-8902, Japan. [7]National Institute of Advanced Industrial Sciences and Technology (AIST), Ibaraki 305-8562, Japan.
*These authors contributed equally to this work.

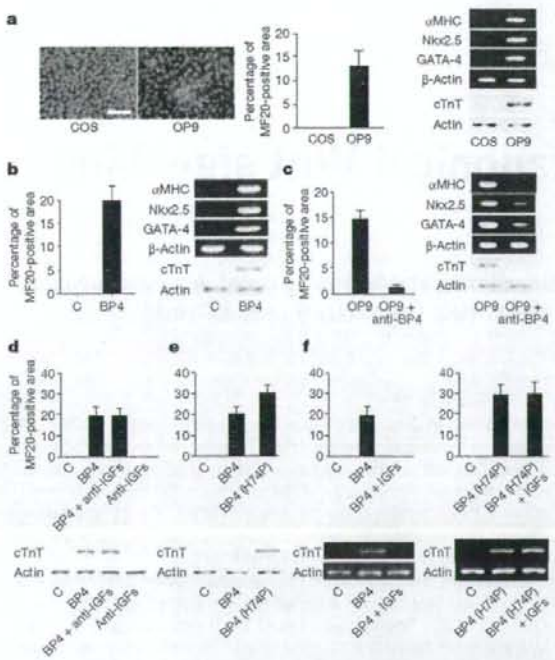

Figure 1 | IGFBP-4 promotes cardiomyocyte differentiation in an IGF-independent manner. a, Culture media conditioned by OP9 cells but not by COS7 cells induced cardiomyocyte differentiation of P19CL6 cells as assessed by MF20-positive area, cardiac marker-gene expression and cTnT protein expression. Scale bar, 100 μm. Error bars show s.d. **b,** Treatment with IGFBP-4 (1 μg ml^{-1}) induced cardiomyocyte differentiation of P19CL6 cells in the absence of DMSO. Error bars show s.d. **c,** Treatment with a neutralizing antibody against IGFBP-4 (anti-BP4; 40 μg ml^{-1}) attenuated cardiomyocyte differentiation of P19CL6 cells induced by OP9-conditioned media. Error bars show s.d. **d,** Treatment with neutralizing antibodies against IGF-I and IGF-II (anti-IGFs; 5 μg ml^{-1} each) had no effect on IGFBP-4-induced cardiomyocyte differentiation of P19CL6 cells. Error bars show s.d. **e,** Mutant IGFBP-4 (BP4(H74P)) that is incapable of binding to IGFs retained cardiomyogenic activity. Error bars show s.d. **f,** IGFs (100 ng ml^{-1} each) attenuated wild-type IGFBP-4-induced but not mutant IGFBP-4-H74P-induced cardiomyocyte differentiation of P19CL6 cells. Error bars show s.d.

that IGFBP-4 induces cardiomyocyte differentiation in an IGF-independent fashion.

To explore further the mechanisms by which IGFBP-4 induces cardiomyogenesis, we tested the hypothesis that IGFBP-4 might modulate the signals activated by other secreted factors implicated in cardiogenesis. It has been shown that canonical Wnt signalling is crucial in cardiomyocyte differentiation[3,4]. In P19CL6 cells, Wnt3A treatment activated β-catenin-dependent transcription of the TOPFLASH reporter gene, and this activation was attenuated by IGFBP-4 (Fig. 2a). Wnt/β-catenin signalling is transduced by the cell-surface receptor complex consisting of Frizzled and low-density-lipoprotein receptor (LDLR)-related protein 5/6 (LRP5/6)[9] and IGFBP-4 attenuated TOPFLASH activity enhanced by the expression of LRP6 or Frizzled 8 (Frz8) (Fig. 2a). As a control, IGFBP-4 did not alter BMP-mediated activation of a BMP-responsive reporter BRE–luc (Supplementary Fig. 1b). These findings suggest that IGFBP-4 is a specific inhibitor of the canonical Wnt pathway. To examine this possibility *in vivo*, we performed axis duplication assays in *Xenopus* embryos. Injection of *Xwnt8* or *Lrp6* mRNA caused secondary axis formation, and injection of *Xenopus IGFBP-4* (*XIGFBP-4*) mRNA alone had minimal effects on axis formation. However, Xwnt8-induced or LRP6-induced secondary axis formation was efficiently blocked by coexpression of XIGFBP-4 (Fig. 2b, c), indicating that IGFBP-4 inhibits canonical Wnt signalling *in vivo*. To explore the mechanisms of Wnt inhibition by IGFBP-4, *Xenopus* animal cap assays and TOPFLASH reporter gene assays were performed. In animal cap assays, IGFBP-4 inhibited LRP6-induced but not β-catenin-induced Wnt-target gene expression (Supplementary Fig. 1c). Similarly, IGFBP-4 attenuated Wnt3A-induced or LRP6-induced TOPFLASH activity but did not alter Dishevelled-1 (Dvl-1)-induced, LiCl-induced or β-catenin-induced TOPFLASH activity (Supplementary Fig. 1d, e). These findings suggest that IGFBP-4 inhibits canonical Wnt signalling at the level of cell-surface receptors. To examine whether IGFBP-4 antagonizes Wnt signalling via direct physical interaction with LRP5/6 or Frizzled, we produced conditioned media containing the Myc-tagged extracellular portion of LRP6 (LRP6N–Myc), the Myc-tagged cysteine-rich domain (CRD) of Frz8 (Frz8CRD–Myc), and V5-tagged IGFBP-4 (IGFBP-4–V5). Immunoprecipitation (IP)/western blot experiments revealed that IGFBP-4 interacted with LRP6N (Fig. 2d) and Frz8CRD (Fig. 2e). A liquid-phase binding assay with ^{125}I-labelled IGFBP-4 and conditioned media containing LRP6N–Myc or Frz8CRD–Myc demonstrated that the interaction between IGFBP-4 and LRP6N or Frz8CRD was specific and saturable (Fig. 2f, g). A Scatchard plot analysis revealed two binding sites with different binding affinities for LRP6N (Fig. 2f, inset) and a single binding site for Frz8CRD (Fig. 2g, inset). A similar binding assay with ^{125}I-labelled Wnt3A demonstrated that IGFBP-4 inhibited Wnt3A binding to LRP6N (Fig. 2h) and Frz8CRD (Fig. 2i), and a Lineweaver–Burk plot revealed that IGFBP-4 was a competitive inhibitor of the binding of Wnt3A to Frz8CDR (Supplementary Fig. 2a). IP/western blot analyses with various deletion mutants of LRP6 and IGFBP-4 revealed that IGFBP-4 interacted with multiple domains of LRP6 and that the carboxy-terminal thyroglobulin domain of IGFBP-4 was required for IGFBP-4 binding to LRP6 or Frz8CRD (Supplementary Fig. 2b–f). It has been shown that inhibition of canonical Wnt signalling promotes cardiomyocyte differentiation in embryonic stem (ES) cells and in chick, *Xenopus* and zebrafish embryos[4,10,11]. These results therefore collectively suggest that IGFBP-4 promotes cardiogenesis by antagonizing the Wnt/β-catenin pathway through direct interactions with Frizzled and LRP5/6.

Next we investigated the role of endogenous IGFBP-4 in P19CL6 cell differentiation into cardiomyocytes. Reverse transcriptase-mediated polymerase chain reaction (RT–PCR) analysis revealed that the expression of *Igfbp4* was upregulated during DMSO-induced P19CL6 cell differentiation (Fig. 3a). Expression of *Igfbp3* and *Igfbp5* was also upregulated in the early and the late phases of differentiation, respectively. Expression of *Igfbp2* was not altered, and that of *Igfbp1* or *Igfbp6* was not detected. When IGFBP-4 was knocked down by two different small interfering RNA (siRNA) constructs, DMSO-induced cardiomyocyte differentiation was inhibited in both cases (Fig. 3b). In contrast, knockdown of *Igfbp3* or *Igfbp5* did not inhibit DMSO-induced cardiomyocyte differentiation (Fig. 3b, right panel). Treatment with an anti-IGFBP-4 neutralizing antibody also blocked DMSO-induced cardiomyocyte differentiation (Fig. 3c). Secretion of endogenous IGFBP-4 is therefore required for the differentiation of P19CL6 cells into cardiomyocytes. Immunostaining for IGFBP-4 revealed that cardiac myocytes were surrounded by the IGFBP-4-positive cells, suggesting that a paracrine effect of IGFBP-4 on cardiomyocyte differentiation is predominant (Fig. 3d). Essentially the same results were obtained in ES cells (Supplementary Fig. 3d–g). To investigate whether IGFBP-4 promotes the differentiation of P19CL6 cells into cardiomyocytes by the inhibition of the canonical Wnt pathway, we expressed dominant-negative LRP6 (LRP6N) in P19CL6 cells. Expression of LRP6N enhanced cardiomyocyte differentiation of P19CL6 cells and reversed the inhibitory effect of *Igfbp4*

knockdown on cardiomyogenesis (Fig. 3e). These observations suggest that endogenous IGFBP-4 is required for cardiomyocyte differentiation of P19CL6 cells and ES cells, and that the cardiogenic effect of IGFBP-4 is mediated by its inhibitory effect on Wnt/β-catenin signalling.

The role of endogenous IGFBP-4 in cardiac development *in vivo* was also examined with *Xenopus* embryos. Whole-mount *in situ* hybridization analysis revealed that strong expression of *XIGFBP-4* was detected at stage 38 in the anterior part of the liver adjacent to the heart (Fig. 4a). Knockdown of *XIGFBP-4* by two different morpholino (MO) constructs resulted in cardiac defects, with more than 70% of the embryos having a small heart or no heart (Fig. 4b). The specificity of MO was confirmed by the observation that simultaneous injection of MO-resistant *XIGFBP-4* cDNA rescued the MO-induced cardiac defects (Fig. 4b, Supplementary Fig. 4c). Coexpression of IGF-binding-defective XIGFBP-4 mutant (XIGFBP-4-H74P) or dominant-negative LRP6 (LRP6N) also rescued the cardiac defects induced by *XIGFBP-4* knockdown (Fig. 4b), whereas overexpression of Xwnt8 in the heart-forming region resulted in cardiac defects similar to those induced by *XIGFBP-4* knockdown (Supplementary Fig. 4d–f), supporting the notion that the cardiogenic effect of IGFBP-4 is independent of IGFs but is mediated by inhibition of the Wnt/β-catenin pathway. The temporal profile of cardiac defects induced by *XIGFBP-4* knockdown was also examined by *in situ* hybridization with *cardiac troponin I* (*cTnI*) (Fig. 4c). At stage 34, morphology of the heart was comparable between control embryos and MO-injected embryos. However, at stage 38, when *XIGFBP-4* starts to be expressed in the anterior part of the liver, the expression of *cTnI* was markedly attenuated in MO-injected embryos; expression of *cTnI* was diminished and no heart-like structure was observed at stage 42. Thus, the heart is initially formed but its subsequent growth is perturbed in the absence of XIGFBP-4, suggesting that IGFBP-4

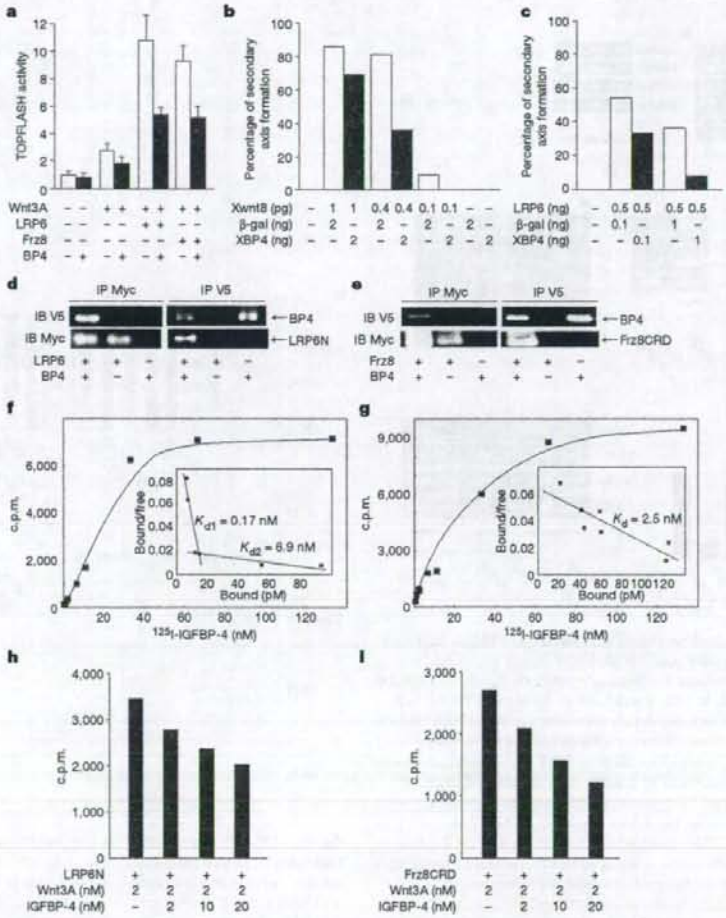

Figure 2 | IGFBP-4 inhibits Wnt/β-catenin signalling through direct interactions with Wnt receptors. **a**, IGFBP-4 attenuated β-catenin-dependent transcription in P19CL6 cells. P19CL6 cells were transfected with TOPFLASH reporter gene and expression vectors for LRP6 or Frz8, and then treated with Wnt3A or Wnt3A plus IGFBP-4; luciferase activities were then measured. Error bars show s.d. **b**, XIGFBP-4 (XBP4) inhibited Xwnt8-induced secondary-axis formation in *Xenopus* embryos (n = 20 for each group). **c**, IGFBP-4 inhibited LRP6-induced secondary-axis formation in *Xenopus* embryos (n = 30 for each group). **d**, **e**, IGFBP-4 interacted directly with LRP6N (**d**) and Frz8CRD (**e**). IB, immunoblotting; IP, immunoprecipitation. **f**, A binding assay between ^{125}I-labelled IGFBP-4 and LRP6N. The inset is a Scatchard plot showing two binding sites with different binding affinities. **g**, A binding assay between ^{125}I-labelled IGFBP-4 and Frz8CRD. The inset is a Scatchard plot showing a single binding site. **h**, **i**, IGFBP-4 inhibited Wnt3A binding to LRP6N (**h**) or Frz8CRD (**i**). ^{125}I-labelled Wnt3A binding to LRP6N or Frz8CRD was assessed in the presence of increasing amounts of IGFBP-4.

promotes cardiogenesis by maintaining the proliferation and/or survival of embryonic cardiomyocytes.

It has been shown that canonical Wnt signals inhibit cardiogenesis in chick and frog embryos, and that Wnt antagonists such as Dkk1 and Crescent secreted from the anterior endoderm or the organizer region counteract the Wnt-mediated inhibitory signals and induce cardiogenesis in the anterior lateral mesoderm[4]. However, IGFBP-4-mediated Wnt inhibition is required at later stages of development, when the heart is already formed at the ventral portion and starts to grow and remodel to maintain embryonic circulation. It has been shown that Wnt/β-catenin signalling has time-dependent effects on cardiogenesis in ES cells: canonical Wnt signalling in the early phase of ES-cell differentiation promotes cardiomyogenesis, whereas it inhibits cardiomyocyte differentiation in the late phase[10–12]. In agreement with this notion, IGFBP-4 promoted cardiomyocyte differentiation of ES cells only when IGFBP-4 was applied in the late phase after embryoid body formation (Supplementary Fig. 3a–c). Similar time-dependent effects of Wnt/β-catenin signalling on cardiogenesis has been shown in zebrafish embryos[11]. Moreover, several recent reports suggest that Wnt/β-catenin signalling is a positive regulator of cardiac progenitor-cell proliferation in the secondary heart field[13]. It therefore seems that canonical Wnt signalling has divergent effects on cardiogenesis at multiple stages of development: first, canonical Wnt signalling promotes cardiogenesis at the time of gastrulation or mesoderm specification; second, it inhibits cardiogenesis at the time when cardiac mesoderm is specified in the anterior lateral mesoderm; third, it promotes the expansion of cardiac progenitors in the secondary heart field; and fourth, it inhibits cardiogenesis at later stages when the embryonic heart is growing. It is interesting to note that IGFBP-4 is expressed predominantly in the liver. Mouse IGFBP-4 is

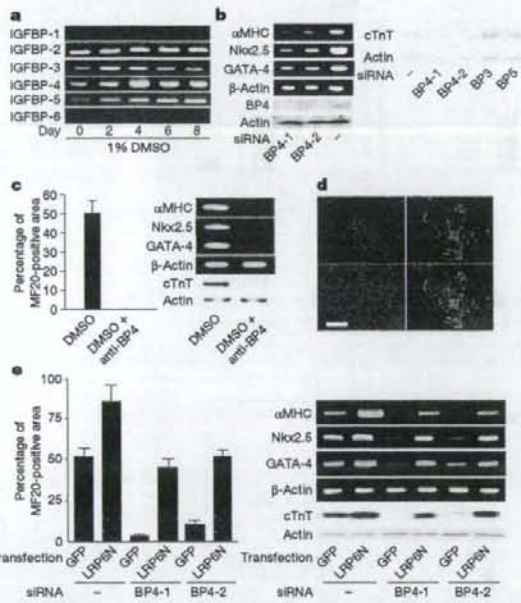

Figure 3 | IGFBP-4 is required for the differentiation of P19CL6 cells into cardiomyocytes. **a**, Expression analysis of IGFBP family members by RT–PCR during DMSO-induced cardiomyocyte differentiation of P19CL6 cells (from day 0 to day 8). **b**, Left: knockdown of *Igfbp4* in P19CL6 cells attenuated cardiac marker expression in response to treatment with DMSO. BP4-1 and BP4-2 represent two different siRNAs for IGFBP-4. Right: knockdown of *Igfbp3* or *Igfbp5* had no effect on cTnT expression in response to DMSO treatment. **c**, Treatment with a neutralizing antibody against IGFBP-4 (anti-BP4; 40 μg ml^{-1}) attenuated DMSO-induced cardiomyocyte differentiation of P19CL6 cells. Error bars show s.d. **d**, IGFBP-4 immunostaining during DMSO-induced differentiation of P19CL6 cells stably transfected with αMHC–green fluorescent protein (GFP) reporter gene. Top left, IGFBP-4 staining (red); top right, GFP expression representing differentiated cardiomyocytes; bottom left, nuclear staining with DAPI (4′,6-diamidino-2-phenylindole); bottom right, a merged picture. Scale bar, 100 μm. **e**, Attenuated cardiomyocyte differentiation of P19CL6 cells by *Igfbp4* knockdown was rescued by inhibiting Wnt/β-catenin signalling. Control and *Igfbp4*-knocked-down P19CL6 cells were transfected with an expression vector for GFP or LRP6N (a dominant-negative form of LRP6) and induced to differentiate into cardiomyocytes by treatment with DMSO. LRP6N overexpression rescued the attenuated cardiomyocyte differentiation induced by *Igfbp4* knockdown as assessed by MF20-positive area (left panel), cardiac marker-gene expression and cTnT protein expression (right panel). Error bars show s.d.

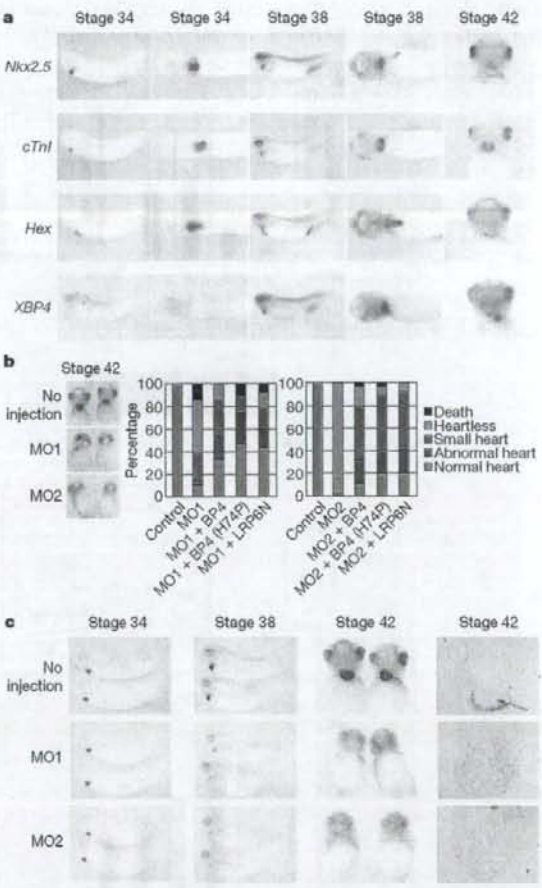

Figure 4 | IGFBP-4 is required for the maturation of the heart in *Xenopus* embryos. **a**, *In situ* hybridization analysis of *Nkx2.5* (an early cardiac marker), *cTnI* (a mature cardiac marker), *Hex* (a liver marker), and *XIGFBP-4* (*XBP4*) mRNA expression at stages 34, 38 and 42. **b**, Knockdown of *XIGFBP-4* by two different morpholinos (MO1 and MO2) resulted in severe cardiac defects as assessed by *cTnI in situ* hybridization at stage 42 (left). These cardiac defects were rescued by simultaneous injection of MO-resistant wild-type XIGFBP-4, mutant XIGFBP-4-H74P (BP4(H74P) and LRP6N ($n = 30$ for each group). **c**, Temporal profile of cardiac defects induced by *XIGFBP-4* knockdown. Morphology of the heart as assessed by cTnI *in situ* hybridization was almost normal at stage 34 but was severely perturbed at stages 38 and 42. The right column shows sections of control and MO-injected embryos. The arrow indicates the heart in control embryos. No heart-like structure was observed in MO-injected embryos.

also strongly expressed in the tissues adjacent to the heart such as pharyngeal arches and liver bud at embryonic day (E)9.5 (Supplementary Fig. 3h). These observations and the results of IGFBP-4 immunostaining in P19CL6 cells and ES cells suggest that IGFBP-4 promotes cardiogenesis in a paracrine fashion. Together with a previous report showing that cardiac mesoderm secretes FGFs and induces liver progenitors in the ventral endoderm[14], these observations suggest that there exist reciprocal paracrine signals between the heart and the liver that coordinately promote the development of each other.

IGFBPs are composed of six members, IGFBP-1 to IGFBP-6. Reporter gene assays and β-catenin stabilization assays revealed that IGFBP-4 was the most potent canonical Wnt inhibitor and that IGFBP-1, IGFBP-2 and IGFBP-6 also showed modest activity in Wnt inhibition, whereas IGFBP-3 and IGFBP-5 had no such activity (Supplementary Fig. 5a–c). In agreement with this, IP/western blot analyses demonstrated that IGFBP-1, IGFBP-2, IGFBP-4 and IGFBP-6 but not IGFBP-3 or IGFBP-5 interacted with LRP6 or Frz8CRD (Supplementary Fig. 5d, e). Thus, the lack of cardiac phenotypes in IGFBP-4-null mice or IGFBP-3/IGFBP-4/IGFBP-5 triple knockout mice[15] may be due to genetic redundancies between IGFBP-4 and other IGFBPs such as IGFBP-1, IGFBP-2 and/or IGFBP-6.

The identification of IGFBP-4 as an inhibitor of Wnt/β-catenin signalling may also have some implications for cancer biology[16]. It was shown that treatment with IGFBP-4 reduces cell proliferation in some cancer cell lines *in vitro*, and that overexpression of IGFBP-4 attenuates the growth of prostate cancer *in vivo*. Decreased serum levels of IGFBP-4 are associated with the risk of breast cancer. Because the activation of Wnt signalling is implicated in several forms of malignant tumours[17,18], it is possible that the inhibitory effect of IGFBP-4 on cell proliferation is mediated in part by the inhibition of canonical Wnt signalling.

METHODS SUMMARY

Cell culture. P19CL6 cells and ES cells were cultured and induced to differentiate into cardiomyocytes essentially as described[9,10]. P19CL6 cells (2,000 cells per 35-mm dish) were treated with various conditioned media for screening of their cardiogenic activities. For siRNA-mediated knockdown, pSIREN-RetroQ vectors (Clontech) ligated with double-stranded oligonucleotides were transfected into P19CL6 cells or ES cells, and puromycin-resistant clones were selected.

IP/western blot analyses and binding assays. Conditioned media for IP/western blot analyses were produced by using 293 cells. Binding reactions were performed overnight at 4 °C. ^{125}I-labelling of IGFBP-4 and Wnt3A was performed with IODO-BEADS Iodination Reagent (Pierce). A liquid-phase binding assay was performed essentially as described[19].

***Xenopus* experiments.** Axis duplication assays, animal cap assays, and *in situ* hybridization analyses in *Xenopus* were performed essentially as described[20]. Electroporation of mRNA was performed at stage 28 essentially as described[21].

Full Methods and any associated references are available in the online version of the paper at www.nature.com/nature.

Received 22 August 2007; accepted 24 April 2008.
Published online 4 Jun 2008.

1. Firth, S. M. & Baxter, R. C. Cellular actions of the insulin-like growth factor binding proteins. *Endocr. Rev.* 23, 824–854 (2002).
2. Mohan, S. & Baylink, D. J. IGF-binding proteins are multifunctional and act via IGF-dependent and -independent mechanisms. *J. Endocrinol.* 175, 19–31 (2002).
3. Olson, E. N. & Schneider, M. D. Sizing up the heart: development redux in disease. *Genes Dev.* 17, 1937–1956 (2003).
4. Foley, A. & Mercola, M. Heart induction: embryology to cardiomyocyte regeneration. *Trends Cardiovasc. Med.* 14, 121–125 (2004).
5. Leri, A., Kajstura, J. & Anversa, P. Cardiac stem cells and mechanisms of myocardial regeneration. *Physiol. Rev.* 85, 1373–1416 (2005).
6. Monzen, K. *et al.* Bone morphogenetic proteins induce cardiomyocyte differentiation through the mitogen-activated protein kinase kinase kinase TAK1 and cardiac transcription factors Csx/Nkx-2.5 and GATA-4. *Mol. Cell. Biol.* 19, 7096–7105 (1999).
7. Ueno, H. *et al.* A stromal cell-derived membrane protein that supports hematopoietic stem cells. *Nature Immunol.* 4, 457–463 (2003).
8. Qin, X., Strong, D. D., Baylink, D. J. & Mohan, S. Structure–function analysis of the human insulin-like growth factor binding protein-4. *J. Biol. Chem.* 273, 23509–23516 (1998).
9. Moon, R. T., Kohn, A. D., De Ferrari, G. V. & Kaykas, A. WNT and β-catenin signalling: diseases and therapies. *Nature Rev. Genet.* 5, 691–701 (2004).
10. Naito, A. T. *et al.* Developmental stage-specific biphasic roles of Wnt/β-catenin signaling in cardiomyogenesis and hematopoiesis. *Proc. Natl Acad. Sci. USA* 103, 19812–19817 (2006).
11. Ueno, S. *et al.* Biphasic role for Wnt/β-catenin signaling in cardiac specification in zebrafish and embryonic stem cells. *Proc. Natl Acad. Sci. USA* 104, 9685–9690 (2007).
12. Liu, Y. *et al.* Sox17 is essential for the specification of cardiac mesoderm in embryonic stem cells. *Proc. Natl Acad. Sci. USA* 104, 3859–3864 (2007).
13. Cohen, E. D., Tian, Y. & Morrisey, E. E. Wnt signaling: an essential regulator of cardiovascular differentiation, morphogenesis and progenitor self-renewal. *Development* 135, 789–798 (2008).
14. Jung, J., Zheng, M., Goldfarb, M. & Zaret, K. S. Initiation of mammalian liver development from endoderm by fibroblast growth factors. *Science* 284, 1998–2003 (1999).
15. Ning, Y. *et al.* Diminished growth and enhanced glucose metabolism in triple knockout mice containing mutations of insulin-like growth factor binding protein-3, -4, and -5. *Mol. Endocrinol.* 20, 2173–2186 (2006).
16. Durai, R. *et al.* Biology of insulin-like growth factor binding protein-4 and its role in cancer. *Int. J. Oncol.* 28, 1317–1325 (2006).
17. Logan, C. Y. & Nusse, R. The Wnt signaling pathway in development and disease. *Annu. Rev. Cell Dev. Biol.* 20, 781–810 (2004).
18. Clevers, H. Wnt/β-catenin signaling in development and disease. *Cell* 127, 469–480 (2006).
19. Semenov, M. V. *et al.* Head inducer Dickkopf-1 is a ligand for Wnt coreceptor LRP6. *Curr. Biol.* 11, 951–961 (2001).
20. Kobayashi, H. *et al.* Novel Daple-like protein positively regulates both the Wnt/β-catenin pathway and the Wnt/JNK pathway in *Xenopus*. *Mech. Dev.* 122, 1138–1153 (2005).
21. Sasagawa, S., Takabatake, T., Takabatake, Y., Muramatsu, T. & Takeshima, K. Improved mRNA electroporation method for *Xenopus* neurula embryos. *Genesis* 33, 81–85 (2002).

Supplementary Information is linked to the online version of the paper at www.nature.com/nature.

Acknowledgements We thank E. Fujita, R. Kobayashi and Y. Ishiyama for technical support; T. Yamauchi and K. Ueki for advice on binding assays; and Y. Onuma and S. Takahashi for advice on *Xenopus* electroporation. This work was supported by grants from the Ministry of Education, Culture, Sports, Science and Technology (MEXT), the Ministry of Health, Labour, and Welfare, and the New Energy and Industrial Technology Development Organization (NEDO).

Author Contributions W.Z., I.S. and Y.I. contributed equally to this work. I.K. designed and supervised the research. W.Z., I.S., Y.I., Z.L., H.I., M.Y. and A.T.N. performed experiments. J.N., H.U., A.U., T.M., T.N., A.K. and M.A. contributed new reagents and/or analytical tools. W.Z., I.S., Y.I., A.K. and I.K. analysed data. W.Z., I.S., Y.I. and I.K. prepared the manuscript.

Author Information Reprints and permissions information is available at www.nature.com/reprints. Correspondence and requests for materials should be addressed to I.K. (komuro-tky@umin.ac.jp).

METHODS

Plasmids and reagents. cDNA clones encoding mouse IGFBPs and *Xenopus* IGFBP-4 were purchased from Open Biosystems. XIGFBP-4-H74P mutant was generated with a QuickChange Site-Directed Mutagenesis kit (Stratagene). His-tagged human wild-type IGFBP-4 and mutant IGFBP-4-H74P (vectors provided by X. Qin)[8] were produced and purified with HisTrap HP Kit (Amersham). Full-length Frz8, Frz8CRD and LRP6N were provided by X. He[22,23]. Full-length LRP6, membrane-bound forms of LRP6 deletion mutants, and Dkk1 were from C. Niehrs[24]. pXwnt8 and pCSKA-Xwnt8 were from J. Christian[25]. pCS2–β-catenin was from D. Kimelman[26]. αMHC–GFP was from B. Fleischmann[27]. BRE–luc was from P. ten Dijke[28]. pCGN-Dvl-1 was described previously[29]. Soluble forms of LRP6 deletion mutants and probes for *in situ* hybridization analysis (Nkx2.5, cTnI and Hex) were generated by PCR. IGFBP-4, Wnt3A, IGF-I, IGF-II and BMP2 were from R&D. Neutralizing antibodies were from R&D (anti-IGFBP-4), Sigma (anti-IGF-I and anti-IGF-II), and Oncogene (anti-type-I IGF receptor). The antibodies used for immunoprecipitation, western blotting and immunostaining were from Invitrogen (anti-Myc, anti-V5), Santa Cruz (anti-cTnT, anti-IGFBP-4, anti-topoisomerase I (TOPO-I)), Sigma (anti-β-actin, anti-β-catenin, anti-FLAG (M2)) and Developmental Studies Hybridoma Bank (anti-sarcomeric myosin heavy chain (MF20)).

Cell culture experiments. P19CL6 cells and ES cells were cultured and induced to differentiate into cardiomyocytes essentially as described[8,10]. P19CL6 cells (2,000 cells per 35-mm dish) were treated with various conditioned media for screening of their cardiogenic activities. P19CL6 cells or ES cells stably transfected with αMHC promoter driven–GFP were generated by transfection of αMHC–GFP plasmid into P19CL6 cells or ht7 ES cells followed by G418 selection. Luciferase reporter gene assays, western blot analyses, immunostaining and RT–PCR were performed as described[10]. Reporter gene assays were repeated at least three times. PCR primers and PCR conditions are listed in Supplementary Table 1. For siRNA-mediated knockdown, siRNAs were expressed with pSIREN-RetroQ vector (Clontech). Oligonucleotide sequences used are listed in Supplementary Table 2. pSIREN-RetroQ vectors ligated with double-stranded oligonucleotides were transfected into P19CL6 cells or ES cells, and puromycin-resistant clones were isolated and expanded. For β-catenin stabilization assays, nuclear extracts of L cells were prepared with NE-PER Nuclear and Cytoplasmic Extraction Reagents (Pierce). Data are shown as means and s.d.

IP/western blot analyses and binding assays. Conditioned media for IP/western blot analyses containing full-length or various deletion mutants of IGFBPs, LRP6, Frz8CRD and Dkk1 were produced with 293 cells. Binding reactions were performed overnight at 4 °C. Immunoprecipitation was performed with Protein G–Sepharose 4 Fast Flow (Amersham). ^{125}I-labelling of IGFBP-4 and Wnt3A was performed with IODO-BEADS Iodination Reagent (Pierce). A liquid-phase binding assay was performed essentially as described[19]. In brief, conditioned media containing LRP6N–Myc or Frz8CRD–Myc were mixed with various concentrations of ^{125}I-labelled IGFBP-4 and incubated overnight at 4 °C. LRP6N–Myc or Frz8CRD–Myc was then immunoprecipitated and the radioactivity of bound IGFBP-4 was measured after extensive washing of the Protein G–Sepharose beads. For a competitive binding assay, conditioned media containing LRP6N–Myc or Frz8CRD–Myc were mixed with ^{125}I-labelled Wnt3A and unlabelled IGFBP-4, and incubated overnight at 4 °C. LRP6N–Myc or Frz8CRD–Myc was then immunoprecipitated and the radioactivity of bound Wnt3A was measured.

***Xenopus* experiments and mouse *in situ* hybridization analysis.** Axis duplication assays, animal cap assays and *in situ* hybridization analyses in *Xenopus* were performed essentially as described[20]. Two independent cDNAs for *XIGFBP-4*, presumably resulting from pseudotetraploid genomes, were identified by 5′ rapid amplification of cDNA ends (Supplementary Fig. 4a). Two different MOs targeting both of these two IGFBP-4 transcripts were designed (Gene Tools) (Supplementary Fig. 4a and Supplementary Table 2). MO-sensitive *XIGFBP-4* cDNA including a 41-base-pair 5′-untranslated region (UTR) was generated by PCR. MO-resistant *XIGFBP-4* cDNA (wild-type and H74P mutant) was generated by introducing five silent mutations in the MO1 target sequence and excluding the 5′-UTR (Supplementary Fig. 4a). To determine the specificity of MOs, MO-sensitive or MO-resistant *XIGFBP-4–myc* mRNA was injected into *Xenopus* embryos with or without MOs, and protein/mRNA expression was analysed. PCR primers and PCR conditions are listed in Supplementary Table 1. MOs and plasmid DNAs were injected at the eight-cell stage into the dorsal region of two dorsal–vegetal blastomeres fated to be heart and liver anlage. Electroporation of mRNA was performed essentially as described[21]. Injection of mRNA (5 ng in 5 nl of solution) into the vicinity of heart anlage and application of electric pulses were performed at stage 28. Whole-mount *in situ* hybridization analysis of murine IGFBP-4 was performed as described[30].

22. He, X. *et al.* A member of the Frizzled protein family mediating axis induction by Wnt-5A. *Science* 275, 1652–1654 (1997).
23. Tamai, K. *et al.* LDL-receptor-related proteins in Wnt signal transduction. *Nature* 407, 530–535 (2000).
24. Mao, B. *et al.* LDL-receptor-related protein 6 is a receptor for Dickkopf proteins. *Nature* 411, 321–325 (2001).
25. Christian, J. L. & Moon, R. T. Interactions between Xwnt-8 and Spemann organizer signaling pathways generate dorsoventral pattern in the embryonic mesoderm of *Xenopus*. *Genes Dev.* 7, 13–28 (1993).
26. Yost, C. *et al.* The axis-inducing activity, stability, and subcellular distribution of β-catenin is regulated in *Xenopus* embryos by glycogen synthase kinase 3. *Genes Dev.* 10, 1443–1454 (1996).
27. Kolossov, E. *et al.* Identification and characterization of embryonic stem cell-derived pacemaker and atrial cardiomyocytes. *FASEB J.* 19, 577–579 (2005).
28. Korchynskyi, O. & ten Dijke, P. Identification and functional characterization of distinct critically important bone morphogenetic protein-specific response elements in the Id1 promoter. *J. Biol. Chem.* 277, 4883–4891 (2002).
29. Kishida, M. *et al.* Synergistic activation of the Wnt signaling pathway by Dvl and casein kinase Iε. *J. Biol. Chem.* 276, 33147–33155 (2001).
30. Hosoda, T. *et al.* A novel myocyte-specific gene Midori promotes the differentiation of P19CL6 cells into cardiomyocytes. *J. Biol. Chem.* 276, 35978–35989 (2001).

STEM CELLS
TISSUE-SPECIFIC STEM CELLS

Novel Cardiac Precursor-Like Cells from Human Menstrual Blood-Derived Mesenchymal Cells

NAOKO HIDA,[a,b,c] NOBUHIRO NISHIYAMA,[a,c] SHUNICHIRO MIYOSHI,[a,d] SHINICHIRO KIRA,[a] KAORU SEGAWA,[e] TARO UYAMA,[b] TAISUKE MORI,[c] KENJI MIYADO,[b] YUKINORI IKEGAMI,[a,b] CHANGHAO CUI,[b] TOHRU KIYONO,[f] SATORU KYO,[g] TATSUYA SHIMIZU,[h] TERUO OKANO,[h] MICHIE SAKAMOTO,[c] SATOSHI OGAWA,[a] AKIHIRO UMEZAWA[b]

[a]Department of Cardiology, Keio University School of Medicine, Tokyo, Japan; [b]Department of Reproductive Biology and Pathology, National Research Institute for Child Health and Development, Tokyo, Japan; [c]Department of Pathology, Keio University School of Medicine, Tokyo, Japan; [d]Institute for Advanced Cardiac Therapeutics, Keio University School of Medicine, Tokyo, Japan; [e]Department of Microbiology and Immunology, Keio University School of Medicine, Tokyo, Japan; [f]Virology Division, National Cancer Center Research Institute, Tokyo, Japan; [g]Department of Obstetrics and Gynecology, Kanazawa University, School of Medicine, Kanazawa, Japan; [h]Institute of Advanced Biomedical Engineering and Science, Tokyo Women's Medical University, Tokyo, Japan

Key Words. Cardiomyogenesis human mesenchymal stem cell • Menstrual blood endometrial gland • Cell sheet technology cardiac precursors

ABSTRACT

Stem cell therapy can help repair damaged heart tissue. Yet many of the suitable cells currently identified for human use are difficult to obtain and involve invasive procedures. In our search for novel stem cells with a higher cardiomyogenic potential than those available from bone marrow, we discovered that potent cardiac precursor-like cells can be harvested from human menstrual blood. This represents a new, noninvasive, and potent source of cardiac stem cell therapeutic material. We demonstrate that menstrual blood-derived mesenchymal cells (MMCs) began beating spontaneously after induction, exhibiting cardiomyocyte-specific action potentials. Cardiac troponin-I-positive cardiomyocytes accounted for 27%–32% of the MMCs in vitro. The MMCs proliferated, on average, 28 generations without affecting cardiomyogenic transdifferentiation ability, and expressed mRNA of GATA-4 before cardiomyogenic induction. Hypothesizing that the majority of cardiomyogenic cells in MMCs originated from detached uterine endometrial glands, we established monoclonal endometrial gland-derived mesenchymal cells (EMCs), 76%–97% of which transdifferentiated into cardiac cells in vitro. Both EMCs and MMCs were positive for CD29, CD105 and negative for CD34, CD45. EMCs engrafted onto a recipient's heart using a novel 3-dimensional EMC cell sheet manipulation transdifferentiated into cardiac tissue layer in vivo. Transplanted MMCs also significantly restored impaired cardiac function, decreasing the myocardial infarction (MI) area in the nude rat model, with tissue of MMC-derived cardiomyocytes observed in the MI area in vivo. Thus, MMCs appear to be a potential novel, easily accessible source of material for cardiac stem cell-based therapy. STEM CELLS *2008;26:1695–1704*

Disclosure of potential conflicts of interest is found at the end of this article.

INTRODUCTION

Marrow-derived mesenchymal stem cells (MSCs) are a potential cellular source for stem cell-based therapy, since they have the ability to differentiate into cardiomyocytes [1, 2], use of MSCs presents no ethical problems, and autologous MSCs have been injected into ischemic hearts clinically [3]. Direct injection of MSCs into the heart has been shown to be feasible in vivo [4–7], but with limited effect. The reason for this may be the extremely low rate of cardiomyogenesis exhibited by marrow-derived MSCs [2], with cardiac function improvement due to grafted MSC-induced neovascularization [7, 8] and an antiapoptotic

Author contributions: N.H.: conception and design, collection and assembly of data, data analysis and interpretation, final approval of manuscript; N.N.: conception and design, collection and assembly of data, data analysis and interpretation, manuscript writing, final approval of manuscript; S.M.: conception and design, administrative support, collection and assembly of data, data analysis and interpretation, manuscript writing, final approval of manuscript; S. Kira and Y.I.: collection and assembly of data, final approval of manuscript; K.S., C.C., T.K., S. Kyo, and T.S.: provision of study material, final approval of manuscript; T.U.: provision of study material, collection and assembly of data, final approval of manuscript; T.M.: collection and assembly of data, data analysis and interpretation, final approval of manuscript; K.M.: collection and assembly of data, final approval of manuscript; T.O.: administrative support, provision of study material, final approval of manuscript; M.S.: administrative support, final approval of manuscript; S.O.: financial support, administrative support, final approval of manuscript; A.U.: financial support, administrative support, manuscript writing, final approval of manuscript.

Correspondence: Shunichiro Miyoshi M.D., Ph.D., Keio University School of Medicine, 35-Shinanomachi, Shinjuku-ku, Tokyo, 160-8582 Japan. Telephone: +81-3-3353-1211 (ext 62310); Fax: +81-3-3353-2502; e-mail: smiyoshi@cpnet.med.keio.ac.jp Received October 2, 2007; accepted for publication April 6, 2008; first published online in STEM CELLS *EXPRESS* April 17, 2008. 1066-5099/2008/$30.00/0 doi: 10.1634/stemcells.2007-0826

effect on infarcted cardiomyocytes [9, 10]. To further improve prospects of restoring cardiac function, a search was initiated for another source of cells having high cardiomyogenic potential.

Our previous study showed that umbilical cord blood-derived mesenchymal stem cells (UCBMSCs) [11] and placental chorionic plate cells (PCPCs) [12] have a phenotype of mesenchymal cells and have higher cardiomyogenic differentiation ability in vitro. Since these materials are deemed medical waste and can be obtained without any ethical problems, they may be a suitable stem cell source for cardiac regenerative therapy. But the population of UCBMSCs in umbilical cord blood is scant [13] and there is also a problem in establishing PCPCs, since placental tissue contains a lot of maternal decidua-derived mesenchymal cells that could contaminate PCPCs. Therefore, it is difficult to obtain enough of these cells without using a limiting dilution method and/or massive ex vivo propagation, which may cause instability of the genome [14]. Consequently, material that contains a large amount of mesenchymal cells during the first few passages should be a highly suitable source of stem cells.

A previous paper suggests that endometrium contains an MSC-like population [15] and menstrual blood-derived mesenchymal (MMCs) cells have a pluripotent differentiation ability in vitro [16]. The data presented here demonstrate that human menstrual blood-derived mesenchymal cells and uterine endometrial gland-derived mesenchymal cells (EMCs) have a strong potential for cardiomyogenic transdifferentiation in vitro and in vivo. Moreover, large amounts of MMCs could be obtained from the first passage of menstrual blood culture, and MMCs have been shown to restore impaired cardiac function through marked cardiomyogenesis in vivo.

Materials and Methods

Isolation of MMCs and EMCs

After informed consent was obtained, mesenchymal cells from approximately 10 ml of menstrual blood of six women (20–30 years old) were collected on the first day of menstruation. The samples were suspended in Dulbecco's modified Eagle's medium (DMEM) high glucose supplemented with 10% FBS, and split into two 10-cm dishes. The estimated adherent cell number at the start of culture was approximately 1×10^7. The growth curve and phase-contrast microscopic view are shown in supplemental online Fig. 1. The results for MMCs obtained from six women were the same. A human endometrial tissue sample was also taken from a 52-year-old woman undergoing hysterectomy [17]. Individual endometrial glands were isolated under a microscope and then seeded. After the retroviral transfection of HPV16E6, E7, and hTERT [2], endometrial cell strains were generated by the limiting dilution method. Two strains exhibiting rapid cell division cycles were designated EMC100 and EMC214 (Fig. 3B and 3D, respectively). EMC100 and EMC214 showed adherent spindle shape morphology that proliferated for more than 250 population doublings without changing cardiomyogenic differentiation ability.

Isolation of Marrow-Derived Mesenchymal Stem Cells

Bone marrow-derived mesenchymal stem cells (BMMSCs) were obtained from a 41-year-old male as described previously [2].

Coculture with Murine Fetal Cardiomyocytes

MMCs, EMCs, and BMMSCs were infected with enhanced green fluorescent protein (EGFP) expressing adenovirus [2]. Fetal cardiomyocytes were obtained from hearts of day-17 mouse fetuses, as previously described [2]. The isolated cardiomyocytes were replated at $5 \times 10^4/cm^2$ on top of a floating athelocollagen membrane (CM-6, 40-μm thickness; Koken, Tokyo, http://www.kokenmpc.co.jp/english/products/collagen/cell_culture/cm-6_24/index.html) that is permeable for only small molecules (less than 5,000 MW). The next day, the athelocollagen membrane was plated upside down on the culture dish. Harvested EGFP-labeled MMCs and EMCs were then seeded upon the athelocollagen surface (bottom surface) at $7 \times 10^3/cm^2$ (Fig. 1M). In several experiments (Figs. 1G–1L, 2, 3E, 3H, 3K–3M, 4, supplemental online Fig. 2, examination of chromosome chimeras), we did not use the athelocollagen membrane for the coculture system.

Immunocytochemistry and Immunohistochemistry

A laser confocal microscope (FV1000; Olympus, Tokyo, http://www.olympus-global.com) was used for immunocytochemical analysis. Samples were stained with mouse monoclonal anti-cardiac troponin-I antibody (4T21 Lot 98/10-T21-C2; HyTest, Euro, Finland, http://www.hytest.fi/) or with mouse monoclonal anti-sarcomeric α-actinin antibody (Sigma-Aldrich, St. Louis, http://www.sigmaaldrich.com), or anti-connexin 43 antibody (Sigma-Aldrich) diluted 1:300 overnight at 4°C, then stained with TRITC-conjugated anti-mouse antibody (Sigma-Aldrich), TRITC-conjugated anti-rabbit antibody (Sigma-Aldrich), and Cy5-conjugated anti-mouse IgG (Chemicon, Temecula, CA, http://www.chemicon.com) diluted 1:100, containing 4′-6-diamidino-2-phenylindole (DAPI; Wako Chemical, Osaka, Japan, http://www.wako-chem.co.jp/english) at 1:300 for 30 minutes at 25°C–28°C. See also supplemental online data 1 for detail of method.

Functional Analysis

The method of action potential (AP) recording was as previously described [2] but with slight modification. A fluorescence inverted microscope (IX-70; Olympus) was used for AP recording. The microscope was equipped with a recording chamber and a noiseless heating plate (Microwarm Plate; Kitazato Supply, Fujinomiya, Shizuoka, Japan, http://www.kitazato-supply.com). A 10-mM volume of HEPES (Sigma-Aldrich) was added to the culture medium to stabilize the pH of the perfusate at 7.5. Standard glass microelectrodes having a direct current resistance of 15–25 MΩ when filled with pipette solution were used. Alexa 568 compound was dissolved to a concentration of 0.5 mM in 2 M of KCl solution in order to completely dissolve the Alexa 568 in the pipette solution. The electrodes were positioned with a motor-driven micromanipulator (PCS-5000; Burleigh Instrument, Inc., New York) under optical control. Spontaneously beating EGFP-positive cells were selected as targets, and after the APs of the target cells had been recorded, the dye was injected by iontophoresis (−7 nA for 10–20 seconds). The extent of dye transfer was monitored under a fluorescence microscope, and digital images were recorded with a digital photo camera (EOS-digital; Canon, Tokyo, http://www.canon.com) mounted on the microscope. The recording pipette was connected to a patch-clamp amplifier (MEZ-8300; Nihon Kohden, Tokyo, http://www.nihonkohden.com). The amplified signal was filtered with a 4-pole Bessel filter (NF-3625; NF electronic instrument; NF Corp., Tokyo, http://www.nfcorp.co.jp/english/index.html) set at 2 kHz, then digitized with an A/D converter with a sampling frequency of 10 kHz (Digidata 1.322A; Molecular Devices Corp., Union City, CA, http://www.moleculardevices.com). Pacemaker potential was defined by the slowly depolarizing membrane potential at phase IV of the AP.

Alexa 568 was injected into cells via recording microelectrodes to stain the cells and confirm that the AP was generated by EGFP-positive cells (Fig. 1G–1I, 3E, 3H). Since the dye did not diffuse into the EGFP-negative murine cardiomyocytes, there were no tight cell-to-cell heterologous connections (i.e., gap junctions), at least in the in vitro condition. In some experiments, Alexa 568 diffused into the EGFP-positive satellite EMCs and MMCs, suggesting that a homologous cell-to-cell connection had been established at least 1 week after cocultivation. The measured parameters of the APs were averaged and are shown in Figure 1K.

The fluorescent image of the beating MMCs and EMCs was monitored using a CCD camera (Ikegami Tsushin Co., Ltd, http://www.ikegami.co.jp) and was stored using digital video. The video images (National Television Standards Committee format, 29.97 frame/second) of contraction of EMCs and MMCs were stored in a personal computer as MPEG-2 format files, then analyzed later.